Journal of Computational Physics 497 (2024) 112610

Contents lists available at ScienceDirect

Journal of Computational Physics

journal homepage: www.elsevier.com/locate/jcp

Unified gas-kinetic wave-particle methods VII: Diatomic gas with rotational and vibrational nonequilibrium

Yufeng Wei [a], Yajun Zhu [a], Kun Xu [a,b,c,*]

[a] Department of Mathematics, Hong Kong University of Science and Technology, Hong Kong, China
[b] Department of Mechanical and Aerospace Engineering, Hong Kong University of Science and Technology, Hong Kong, China
[c] HKUST Shenzhen Research Institute, Shenzhen, 518057, China

ARTICLE INFO

Keywords:
Wave-particle decomposition
Molecular vibration
Multiscale modeling
Non-equilibrium flow
Hypersonic flow

ABSTRACT

Hypersonic flow around a vehicle in near space flight is associated with multiscale non-equilibrium physics at a large variation of local Knudsen number from the leading edge highly compressible flow to the trailing edge particle free transport. To accurately capture the solution in all flow regimes from the continuum Navier–Stokes solution to the rarefied gas dynamics in a single computation requires genuinely multiscale method. The unified gas-kinetic wave-particle (UGKWP) method targets on the simulation of such a multiscale transport. Due to the wave-particle decomposition, the dynamics in the Navier–Stokes wave and kinetic particle transport has been unified systematically and efficiently under the unified gas-kinetic scheme (UGKS) framework. In this study, the UGKWP method with the non-equilibrium among translation, rotation and vibration modes, is developed based on a multiple temperature relaxation model. The real gas effect for high speed flow in different flow regimes has been properly captured. Numerical tests, including Sod tube, normal shock structure, hypersonic flow around two-dimensional cylinder and three-dimensional flow around a sphere and space vehicle, have been conducted to validate the UGKWP method. In comparison with the discrete velocity method (DVM)-based Boltzmann solver and particle-based direct simulation Monte Carlo (DSMC) method, the UGKWP method shows remarkable advantages in terms of computational efficiency, memory reduction, and automatic recovering of multiscale solution in the high speed flow simulations.

1. Introduction

For high-speed flying vehicle in near space, the highly compressed gas at the leading edge and the strong expansion wave in the trailing edge can cover the whole flow regimes with several orders of magnitude on the differences of particle mean free path [1]. Multiscale flow with a large variation of local Knudsen number is involved in the computation of the flow field around the vehicle. For high-speed and high-temperature flow, both rotational and vibrational modes of diatomic gas will be activated with significant impact on aerodynamic heating and resistance [2]. In the aerospace engineering practice, an accurate and efficient multiscale method

* Corresponding author at: Department of Mathematics, Hong Kong University of Science and Technology, Hong Kong, China.
E-mail address: makxu@ust.hk (K. Xu).

https://doi.org/10.1016/j.jcp.2023.112610
Received 28 November 2022; Received in revised form 23 October 2023; Accepted 27 October 2023

Available online 31 October 2023

being capable of simulating both continuum and rarefied flow with the inclusion of molecular translation, rotation, and vibration nonequilibrium is of great importance.

The Boltzmann equation is the fundamental governing equation in rarefied gas dynamics. Theoretically, it can capture multiscale flow physics in all Knudsen regimes, with the enforcement of resolving the flow physics in the particle mean free path and mean collision time scale. For highly non-equilibrium flow, there are mainly two kinds of numerical methods to solve the Boltzmann equation, i.e., the stochastic particle method and the deterministic discrete velocity method. The stochastic methods employ discrete particles to simulate the statistical behavior of molecular gas dynamics [1,3–11]. This kind of Lagrangian-type scheme achieves high computational efficiency and robustness in rarefied flow simulation, especially for hypersonic flow. However, it suffers from statistical noise in the low-speed simulation due to its intrinsic stochastic nature. Meanwhile, in the near continuum flow regime, the treatment of intensive particle collisions makes the computational cost very high. The deterministic approaches apply a discrete distribution function to solve the kinetic equations and naturally obtain accurate solutions without statistical noise [12–25]. At the same time, the deterministic method can achieve high efficiency by using numerical acceleration techniques, such as implicit algorithms [14,26–30], memory reduction techniques [24], and adaptive refinement method [31], fast evaluation of the Boltzmann collision term [32,33]. Asymptotic preserving (AP) schemes [34,35] can be developed to release the stiffness of the collision term at the small Knudsen number case. However, for most AP schemes only the Euler solution in the hydrodynamic limit is recovered. In order to recover the Navier-Stokes solution in the continuum regime, the scheme has to possess the unified preserving (UP) property [36]. Additionally, for hypersonic and rarefied flow, the deterministic methods have to discretize the particle velocity space with a high resolution to capture nonequilibrium distribution, which brings huge memory consumption and computational cost, especially for the three-dimensional calculation. Moreover, for both stochastic and deterministic methods, once the gas evolution process is split into collisionless free transport and instant collision, a numerical dissipation being proportional to the time step is usually unavoidable. Therefore, the mesh size and the time step in these schemes have to be less than the mean free path and the particle mean collision time, respectively, to avoid the physical dissipation being overwhelmingly taken over by the numerical one in the continuum regime, such as the laminar boundary layer computation at high Reynolds number. In order to remove the constraints on the mesh size and time step in the continuum flow regime, the unified gas-kinetic scheme (UGKS) and discrete UGKS (DUGKS) with the coupled particle transport and collision in the flux evaluation have been constructed successfully with UP property [18,30,36,37]. At the same time, the multiscale particle methods have been constructed as well [38,39].

Combining the advantages of the deterministic and the stochastic methods, a unified gas-kinetic wave-particle (UGKWP) method [40,41] was proposed under the UGKS framework [42], as well as the simplified versions [43,44]. The coupled multiscale transport and collision in UGKWP is modeled according to cell's Knudsen number and is used in the flux evaluation across the cell interface and inner cell relaxation. The UGKWP method releases the restriction on the mesh size and time step being less than the particle mean free path and particle collision time. Also, the wave-particle decomposition in UGKWP makes the scheme adaptively become a particle method in highly rarefied flow regime and a hydrodynamic flow solver in the continuum flow regime. In the continuum flow limit at a small cell's Knudsen number, the UGKWP gets back to the gas kinetic scheme (GKS) for the Navier–Stokes solution [45]. Thus, the UGKWP method could achieve high efficiency both in the continuum and rarefied regimes. In the intermediate transition regime, the distributions of wave and particle are fully controlled by the time accurate integral solution of the kinetic model equation. Different from the hybrid methods with domain decompositions for different solvers with interfaces to separate them, the UGKWP method employs an adaptive wave-particle decomposition in each cell with a unified treatment in the whole computational domain. The contributions of wave and particle are weighted by the local Knudsen number ($\mathrm{Kn}_c = \tau/\Delta t$) defined by the ratio of particle collision time τ over the numerical time step Δt, with the weights $\exp(-\mathrm{Kn}_c)$ and $(1-\exp(-\mathrm{Kn}_c))$. As a result, the UGKWP method becomes a physically consistent and numerically efficient solver for multiscale flow. The methodology of UGKWP has been extended to other multiscale transport processes, such as radiation, plasma, and multiphase flow [46–50].

In the previous works [40,41], the Bhatnagar–Gross–Krook (BGK) [51] model and Shakhov model [52] were employed to describe the multiscale evolution of monatomic gas flow. For diatomic gases, the internal degrees of freedom, such as rotation and vibration, should be considered [48,53–58], especially for the high-speed and high-temperature flow. The BGK-type model was extended to diatomic gas by introducing additional internal energy variables in the distribution function [54,59–62]. The Rykov model [60] was also incorporated in the UGKWP method to include the diatomic effect with molecular translational and rotational nonequilibrium only [48]. In this study, we present the UGKWP method with the inclusion of vibrational mode for diatomic gas. The vibrational model is used to describe the relaxation process from non-equilibrium to the equilibrium state [1], where three equilibrium states are employed to take into account of the elastic and inelastic collisions and the detailed energy exchange between the translational, rotational and vibrational degrees of freedom. With the inclusion of molecular vibrational mode, the UGKWP method has to take into account several groups of particles with different temperature. But, it provides more accurate solution for multiscale transport for high-speed and high-temperature flow. In this paper, in order to clearly present the algorithm development, the scheme with the BGK-type relaxation model will be constructed and validated in many cases from one dimensional to three dimensional flow simulations. The scheme with the inclusion of additional heat flux modification through the Shakhov and Rykov models can be done easily under the current framework.

The paper is organized as follows. Section 2 presents the kinetic model of diatomic gas with molecular vibration. Since the UGKWP method has adaptive wave-particle decomposition and is an enhanced unified gas-kinetic particle (UGKP), the UGKP method will be introduced first in Section 3. Then the UGKWP method with molecular vibration will be presented in Section 4. Numerical validation of the current method will be carried out in Section 5 and a conclusion will be drawn in Section 6.

2. Kinetic model equation for diatomic gas

2.1. Kinetic model with molecular translation, rotation and vibration

Considering molecular rotation and vibration, the kinetic model equation for diatomic gases can be written as

$$\frac{\partial f}{\partial t}+\boldsymbol{u}\cdot\frac{\partial f}{\partial \boldsymbol{r}}=\frac{g_t-f}{\tau}+\frac{g_{tr}-g_t}{Z_r\tau}+\frac{g_M-g_{tr}}{Z_v\tau}, \tag{1}$$

where $f=f\left(\boldsymbol{r},\boldsymbol{u},\boldsymbol{\xi},\varepsilon_v,t\right)$ is the distribution function for gas molecules at physical space location $\boldsymbol{r}$ with microscopic translational velocity $\boldsymbol{u}$, rotational motion $\boldsymbol{\xi}$, and vibrational energy ε_v at time t. τ is the mean collision time or relaxation time to represent the mean time interval of two successive collisions. The rotational and vibrational relaxation times are defined as

$$\tau_{rot}=Z_r\tau,$$

$$\tau_{vib}=Z_v\tau,$$

where Z_r and Z_v are the rotational and vibration collision numbers, respectively.

The elastic collision process of molecules' translational motions and the inelastic collision process of internal energy exchange are described by the right-hand side of Eq. (1) with three equilibrium states. The equilibrium state g_t with three different temperatures for molecular translation, rotation and vibration gives

$$g_t=\rho\left(\frac{\lambda_t}{\pi}\right)^{\frac{3}{2}}e^{-\lambda_t c^2}\left(\frac{\lambda_r}{\pi}\right)e^{-\lambda_r\xi^2}\frac{4\lambda_v}{K_v(\lambda_v)}e^{-\frac{4\lambda_v}{K_v(\lambda_v)}\varepsilon_v},$$

where $\boldsymbol{c}=\boldsymbol{u}-\boldsymbol{U}$ denotes the peculiar velocity, and $c^2=(u-U)^2+(v-V)^2+(w-W)^2$ and $\boldsymbol{\xi}^2=\xi_1^2+\xi_2^2$. The intermediate equilibrium state g_{tr} has the same temperature λ_{tr} of molecular translation and rotation, but a different temperature λ_v for vibration, which indicates complete energy exchange between translational and rotational degrees of freedom, and a frozen process of vibrational energy

$$g_{tr}=\rho\left(\frac{\lambda_{tr}}{\pi}\right)^{\frac{3}{2}}e^{-\lambda_{tr}c^2}\left(\frac{\lambda_{tr}}{\pi}\right)e^{-\lambda_{tr}\xi^2}\frac{4\lambda_v}{K_v(\lambda_v)}e^{-\frac{4\lambda_v}{K_v(\lambda_v)}\varepsilon_v}.$$

After sufficient collisions, the equilibrium state with equal-partitioned energy for each degree of freedom

$$g_M=\rho\left(\frac{\lambda_M}{\pi}\right)^{\frac{3}{2}}e^{-\lambda_M c^2}\left(\frac{\lambda_M}{\pi}\right)e^{-\lambda_M\xi^2}\frac{4\lambda_M}{K_v(\lambda_M)}e^{-\frac{4\lambda_M}{K_v(\lambda_M)}\varepsilon_v}$$

will be reached.

In these equilibrium states, λ is computed from the corresponding internal energy. Specifically, we have

$$\lambda_t=\frac{3\rho}{4}/(\rho E_t),$$

$$\lambda_r=\frac{K_r\rho}{4}/(\rho E_r),$$

$$\lambda_v=\frac{K_v(\lambda_v)\rho}{4}/(\rho E_v),$$

$$\lambda_{tr}=\frac{(3+K_r)\rho}{4}/(\rho E_{tr}),$$

$$\lambda_M=\frac{[3+K_r+K_v(\lambda_M)]\rho}{4}/(\rho E_M),$$

and

$$\rho E_t=\frac{1}{2}\int \boldsymbol{c}^2 f\,\mathrm{d}\boldsymbol{\Xi},$$

$$\rho E_r=\frac{1}{2}\int \boldsymbol{\xi}^2 f\,\mathrm{d}\boldsymbol{\Xi},$$

$$\rho E_v=\int \varepsilon_v f\,\mathrm{d}\boldsymbol{\Xi},$$

$$\rho E_{tr}=\frac{1}{2}\int (\boldsymbol{c}^2+\boldsymbol{\xi}^2) f\,\mathrm{d}\boldsymbol{\Xi},$$

$$\rho E_M=\int \left[\frac{1}{2}(\boldsymbol{c}^2+\boldsymbol{\xi}^2)+\varepsilon_v\right] f\,\mathrm{d}\boldsymbol{\Xi},$$

where

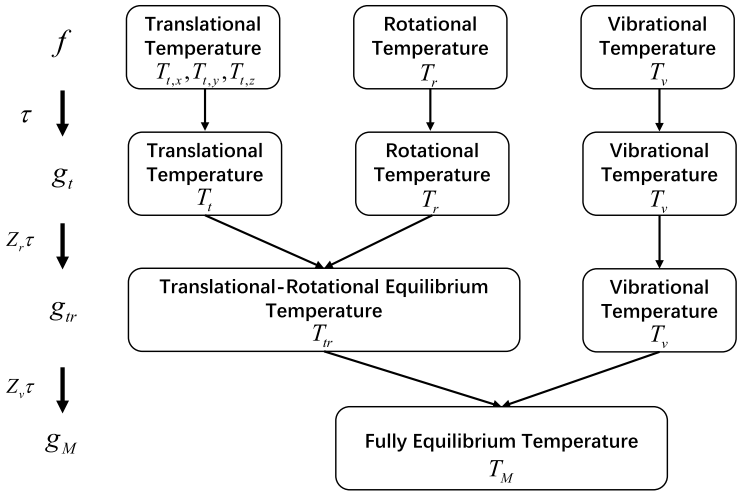

Fig. 1. Relaxation process for the vibrational model.

$$\int (\cdot)\mathrm{d}\boldsymbol{\Xi} = \int_{-\infty}^{\infty} \mathrm{d}\boldsymbol{u} \int_{-\infty}^{\infty} \mathrm{d}\boldsymbol{\xi} \int_{0}^{\infty} (\cdot)\mathrm{d}\varepsilon_v,$$

and K_r and $K_v(\lambda)$ denote the number of rotational and vibrational degrees of freedom, respectively. λ_t, λ_r, λ_v, λ_{tr}, λ_M are associated with the translational temperature T_t, rotational temperature T_r, vibrational temperature T_v, the translation-rotation average temperature T_{tr} and the fully relaxed temperature T_M, respectively by $\lambda = m/(2k_B T)$, where m is molecular mass, k_B is the Boltzmann constant. It should be noted that the number of vibrational degrees of freedom $K_v(\lambda)$ is determined by the vibrational temperature in each equilibrium state, i.e.,

$$K_v(\lambda) = \frac{4\Theta_v k_B \lambda/m}{e^{2\Theta_v k_B \lambda/m} - 1}, \tag{2}$$

where Θ_v is the characteristic temperature of vibration for diatomic gases, e.g., 3371 K for nitrogen and 2256 K for oxygen [4].

With the above three equilibrium states, the energy exchange between molecular translation, rotation, and vibration can be well described by adjusting the collision numbers Z_r and Z_v. Experimental observation shows that the rotational relaxation is faster than the vibrational one, i.e., $1 < Z_r < Z_v$. From the relaxation terms on the right-hand side of Eq. (1), the relaxation process can be divided into three stages as shown in Fig. 1. Firstly, the non-equilibrium distribution function f has different translational, rotational, and vibrational temperatures. After time τ, the elastic collisions drive the distribution function f approaching the translational equilibrium state g_t. In the second stage, the inelastic collisions happen within time $Z_r\tau$ to exchange the translational and rotational energy, which drives the distribution function approaching the rotational equilibrium state g_{tr} with the same translational and rotational temperature T_{tr}. In the last stage, gas molecules encounter sufficient elastic and inelastic collisions within time $Z_v\tau$, and the internal energy is fully exchanged between each degree of freedom. At this time, the full equilibrium state g_M with the same temperature T_M for translation, rotation, and vibration is achieved.

3. Unified gas-kinetic particle method

3.1. General framework

The unified gas-kinetic particle (UGKP) method is a particle implementation of the UGKS under the finite volume framework, where the discrete particles are employed to describe the non-equilibrium gas distribution function, and the evolution of particles recovers the multiscale nature in different flow regimes.

Here, we re-write the kinetic model equation in a BGK-type as

$$\frac{\partial f}{\partial t} + \boldsymbol{u} \cdot \frac{\partial f}{\partial \boldsymbol{r}} = \frac{g^* - f}{\tau}, \tag{3}$$

where g^* is the effective equilibrium state, defined as the convex combination of three modified equilibrium distribution function

$$g^* = \left(1 - \frac{1}{Z_r}\right) g_t + \left(\frac{1}{Z_r} - \frac{1}{Z_v}\right) g_{tr} + \frac{1}{Z_v} g_M. \tag{4}$$

Along the characteristic line, the integral solution of the kinetic model equation gives

$$f(\boldsymbol{r},t)=\frac{1}{\tau}\int_0^t e^{-(t-t')/\tau}g^*(\boldsymbol{r}',t')\mathrm{d}t'+e^{-t/\tau}f_0(\boldsymbol{r}-\boldsymbol{u}t), \tag{5}$$

where $f_0(\boldsymbol{r})$ is the initial distribution function at the beginning of each step t_n, and $g^*(\boldsymbol{r},t)$ is the effective equilibrium state distributed in space and time around $\boldsymbol{r}$ and t. The integral solution describes an evolution process from non-equilibrium to equilibrium state through particle collision.

In the UGKS, with the expansion of initial distribution function and equilibrium state

$$\begin{aligned} f_0(\boldsymbol{r}) &= f_0+\boldsymbol{r}\cdot\frac{\partial f}{\partial \boldsymbol{r}},\\ g^*(\boldsymbol{r},t) &= g_0^*+\boldsymbol{r}\cdot\frac{\partial g^*}{\partial \boldsymbol{r}}+\frac{\partial g^*}{\partial t}t, \end{aligned} \tag{6}$$

the second-order accurate flux for macroscopic flow variables across cell interface ij can be constructed from the integral solution

$$\begin{aligned} \boldsymbol{F}_{ij} &= \frac{1}{\Delta t}\int_0^{\Delta t}\int \boldsymbol{u}\cdot\boldsymbol{n}_{ij}f_{ij}(t)\boldsymbol{\psi}\mathrm{d}\Xi\mathrm{d}t\\ &= \int \boldsymbol{u}\cdot\boldsymbol{n}_{ij}\left[C_1g_0^*+C_2\boldsymbol{u}\cdot\frac{\partial g^*}{\partial \boldsymbol{r}}+C_3\frac{\partial g^*}{\partial t}\right]\boldsymbol{\psi}\mathrm{d}\Xi+\int \boldsymbol{u}\cdot\boldsymbol{n}_{ij}\left[C_4f_0+C_5\boldsymbol{u}\cdot\frac{\partial f}{\partial \boldsymbol{r}}\right]\boldsymbol{\psi}\mathrm{d}\Xi\\ &= \boldsymbol{F}_{ij}^{eq}+\boldsymbol{F}_{ij}^{fr} \end{aligned} \tag{7}$$

where $\boldsymbol{n}_{ij}$ is the normal vector of the cell interface, and

$$\boldsymbol{\psi}=\left(1,\boldsymbol{u},\frac{1}{2}\boldsymbol{u}^2+\frac{1}{2}\xi^2+\varepsilon_v,\frac{1}{2}\xi^2,\varepsilon_v\right)^T.$$

$\boldsymbol{F}_{ij}^{fr}$ and $\boldsymbol{F}_{ij}^{eq}$ are the macroscopic fluxes in the free transport and collision processes, respectively. The integrated time coefficients are

$$\begin{aligned} C_1 &= 1-\frac{\tau}{\Delta t}\left(1-e^{-\Delta t/\tau}\right),\\ C_2 &= -\tau+\frac{2\tau^2}{\Delta t}-e^{-\Delta t/\tau}\left(\frac{2\tau^2}{\Delta t}+\tau\right),\\ C_3 &= \frac{1}{2}\Delta t-\tau+\frac{\tau^2}{\Delta t}\left(1-e^{-\Delta t/\tau}\right),\\ C_4 &= \frac{\tau}{\Delta t}\left(1-e^{-\Delta t/\tau}\right),\\ C_5 &= \tau e^{-\Delta t/\tau}-\frac{\tau^2}{\Delta t}(1-e^{-\Delta t/\tau}). \end{aligned}$$

The UGKS updates both the gas distribution function and macroscopic flow variables under a finite volume framework. In the UGKP method, the particle will be used to follow the evolution of gas distribution function directly and keep the finite volume version for the updates of macroscopic flow variables. On the microscopic scale, the particle evolution follows the evolution solution in Eq. (5), where the particle free transport and collision will be taken into account. On the macroscopic scale, the fluxes across the cell interface for the updates of macroscopic flow variables inside each control volume are evaluated by Eq. (7).

Denote a simulation particle as $P_k(m_k,\boldsymbol{r}_k,\boldsymbol{u}_k,e_{r,k},e_{v,k})$, which represents a package of real gas molecules at location $\boldsymbol{r}_k$ with particle mass m_k, microscopic velocity $\boldsymbol{u}_k$, rotational energy $e_{r,k}$ and vibrational energy $e_{v,k}$. According to the integral solution, the cumulative distribution function of particle's collision is

$$\mathcal{G}(t)=1-\exp(-t/\tau),$$

then the free transport time of a particle within one time step Δt would be

$$t_f=\min(-\tau\ln\eta,\Delta t), \tag{8}$$

where η is a random number uniformly distributed in $(0,1)$. In a numerical time step from t^n to t^{n+1}, according to the free transport time t_f, the simulation particles can be categorized into collisionless particles ($t_f=\Delta t$) and collisional particles ($t_f<\Delta t$).

In the free transport process, i.e., $t<t_f$, no collisions would happen, and the particles move freely and carry the initial information. The trajectory of particle P_k could be fully tracked by

$$\boldsymbol{x}_k=\boldsymbol{x}_k^n+\boldsymbol{u}_kt_{f,k}. \tag{9}$$

During the free transport process, the effective net flux across interfaces of cell i can be evaluated by

$$\boldsymbol{F}_i^{fr} = \frac{1}{\Delta t}\left(- \sum_{k \in P_{\partial\Omega_i^{in}}} \boldsymbol{\phi}_k + \sum_{k \in P_{\partial\Omega_i^{out}}} \boldsymbol{\phi}_k \right), \tag{10}$$

where $\boldsymbol{\phi}_k = (m_k, m_k \boldsymbol{u}_k, \frac{1}{2} m_k \boldsymbol{u}_k^2 + m_k e_r + m_k e_v, m_k e_r, m_k e_v)^T$, $P_{\partial\Omega_i^{out}}$ is the index set of the particles streaming out of the volume Ω_i in the outward normal direction during a time step, and $P_{\partial\Omega_i^{in}}$ is the index set of the particles streaming into the volume Ω_i. The free transport flux $\boldsymbol{F}_{ij}^{fr}$ in Eq. (7) has been recovered by the particles' movement.

In the free transport process, the particle during the time interval $(0, t_f)$ is fully tracked. The collisionless particles with $t_f = \Delta t$ are kept at the end of the time step. The collisional particles with $t_f < \Delta t$ would encounter collision at t_f and they are only tracked up to this moment. Then, all collisional particles are removed, but their accumulating mass, momentum, and energy inside each cell can be still updated through the evolution of macroscopic variables. These collisional particles can be re-sampled from the updated macroscopic variables at the beginning of next time step from equilibrium state if needed.

The equilibrium flux $\boldsymbol{F}_{ij}^{eq}$ in Eq. (7) contains three terms, i.e., g^*, $\partial_{\boldsymbol{r}} g^*$ and $\partial_t g^*$, which are only related to the equilibrium states and can be fully determined by the macroscopic flow variables. Here we re-write Eq. (4) as

$$g^* = g_t + \frac{g_{tr} - g_t}{Z_r} + \frac{g_M - g_{tr}}{Z_v}.$$

The previous study [48] shows that

$$\frac{g_{tr} - g_t}{Z_r} = \mathcal{O}(\tau), \quad \frac{g_M - g_{tr}}{Z_v} = \mathcal{O}(\tau), \quad \tau \to 0.$$

Therefore, the terms with coefficients C_2 and C_3 in the equilibrium flux related to the spatial and temporal gradients $\partial_{\boldsymbol{r}} g^*$ and $\partial_t g^*$ would be on the order of $\mathcal{O}(\tau^2)$ or $\mathcal{O}(\tau \Delta t)$, which can be ignored in the continuum regime $\Delta t > \tau$ for recovering NS limit.

Once the Maxwellian distribution and its derivatives around the cell interface are determined, the equilibrium flux $\boldsymbol{F}_{ij}^{eq}$ can be obtained by

$$\boldsymbol{F}_{ij}^{eq} = \int \boldsymbol{u} \cdot \boldsymbol{n}_{ij} \left[C_1 g_0^* + C_2 \boldsymbol{u} \cdot \frac{\partial g_t}{\partial \boldsymbol{r}} + C_3 \frac{\partial g_t}{\partial t} \right] \boldsymbol{\psi} \mathrm{d}\boldsymbol{\Xi}. \tag{11}$$

The macroscopic variables for the determination of equilibrium state g_0^* at cell interface ij are coming from the colliding particles from both sides of the cell interface

$$\boldsymbol{W}_{ij} = \int \left[g_t^l H[\bar{u}_{ij}] + g_t^r (1 - H[\bar{u}_{ij}]) \right] \boldsymbol{\psi} \mathrm{d}\boldsymbol{\Xi},$$

where $\bar{u}_{ij} = \boldsymbol{u} \cdot \boldsymbol{n}_{ij}$, and $H[x]$ is the Heaviside function. The gradient of the equilibrium state is obtained from the gradient of macroscopic flow variables $\partial \boldsymbol{W}_{ij} / \partial \boldsymbol{r}$, see Appendix A. In this study, the spatial reconstruction of macroscopic flow variables is carried out by the least-square method with Venkatakrishnan limiter [63]. As to the temporal gradient, the compatibility condition on Eq. (3)

$$\int (g_t - f) \boldsymbol{\psi} \mathrm{d}\boldsymbol{\Xi} = 0$$

is employed to give

$$\frac{\partial \boldsymbol{W}_{ij}}{\partial t} = - \int \boldsymbol{u} \cdot \frac{\partial g_t}{\partial \boldsymbol{r}} \boldsymbol{\psi} \mathrm{d}\boldsymbol{\Xi}.$$

Correspondingly, the temporal gradient of equilibrium state $\partial_t g_t$ can be evaluated from the above $\partial \boldsymbol{W}_{ij} / \partial t$. With g_0^*, $\partial_{\boldsymbol{r}} g_t$ and $\partial_t g_t$, the equilibrium flux $\boldsymbol{F}_{ij}^{eq}$ can be fully determined.

During the collision process, inelastic collisions will happen, which lead to energy exchange between the degrees of freedom of molecular translation, rotation and vibration. As a result, source terms appear in the macroscopic governing equations, i.e.,

$$\boldsymbol{S} = \int_{t^n}^{t^{n+1}} \frac{g^* - f}{\tau} \boldsymbol{\psi} \mathrm{d}\boldsymbol{\Xi} \mathrm{d}t = \int_{t^n}^{t^{n+1}} \boldsymbol{s} \mathrm{d}t, \tag{12}$$

where $\boldsymbol{s}$ can be expressed as

$$\boldsymbol{s} = \left(0, \boldsymbol{0}, 0, \frac{\rho E_r^{tr} - \rho E_r}{Z_r \tau} + \frac{\rho E_r^M - \rho E_r^{tr}}{Z_v \tau}, \frac{\rho E_v^M - \rho E_v}{Z_v \tau} \right)^T.$$

The intermediate equilibrium energy ρE_r^{tr} is determined under the assumption $\lambda_r = \lambda_t = \lambda_{tr}$, and thus

$$\rho E_r^{tr} = \frac{K_r \rho}{4 \lambda_{tr}}, \qquad \lambda_{tr} = \frac{(K_r + 3)\rho}{4(\rho E - \frac{1}{2}\rho \boldsymbol{U}^2 - \rho E_v)}. \tag{13}$$

The rotational and vibrational energy at the full equilibrium state ρE_r^M and ρE_v^M are determined under the assumption $\lambda_v = \lambda_r = \lambda_t = \lambda_M$, and thus

$$\rho E_r^M = \frac{K_r \rho}{4\lambda_M}, \quad \rho E_v^M = \frac{K_v(\lambda_M)\rho}{4\lambda_M} \quad \text{and} \quad \lambda_M = \frac{\left(K_v(\lambda_M) + K_r + 3\right)\rho}{4\left(\rho E - \frac{1}{2}\rho \boldsymbol{U}^2\right)}. \tag{14}$$

With consideration of numerical stability, the source term is usually treated in an implicit way, such as the trapezoidal rule for rotational and vibrational energies

$$\begin{aligned} S_r &= \frac{\Delta t}{2}\left(s_r^n + s_r^{n+1}\right) \\ &= \frac{\Delta t}{2}\left[\frac{(\rho E_r^{tr})^n - (\rho E_r)^n}{Z_r \tau} + \frac{(\rho E_r^M)^n - (\rho E_r^{tr})^n}{Z_v \tau}\right] \\ &+ \frac{\Delta t}{2}\left[\frac{(\rho E_r^{tr})^{n+1} - (\rho E_r)^{n+1}}{Z_r \tau} + \frac{(\rho E_r^M)^{n+1} - (\rho E_r^{tr})^{n+1}}{Z_v \tau}\right], \\ S_v &= \frac{\Delta t}{2}\left(s_v^n + s_v^{n+1}\right) = \frac{\Delta t}{2}\left[\frac{(\rho E_v^M)^n - (\rho E_v)^n}{Z_v \tau} + \frac{(\rho E_v^M)^{n+1} - (\rho E_v)^{n+1}}{Z_v \tau}\right]. \end{aligned}$$

3.2. Updates of macroscopic variables and discrete particles

Under the finite volume framework, according to the conservation law, the updates of macroscopic variables can be written as

$$\boldsymbol{W}_i^{n+1} = \boldsymbol{W}_i^n - \frac{\Delta t}{\Omega_i}\sum_{j \in N(i)} \boldsymbol{F}_{ij}^{eq} \mathcal{A}_{ij} - \frac{\Delta t}{\Omega_i}\boldsymbol{F}_i^{fr} + \boldsymbol{S}_i, \tag{15}$$

where $\boldsymbol{F}_i^{fr}$ is the net free streaming flow of cell i calculated by particle tracking in the free transport process in Eq. (10), the equilibrium flux $\boldsymbol{F}_{ij}^{eq}$ is evaluated from macroscopic flow variables and their gradients in Eq. (11), and the source term $\boldsymbol{S}_i$ in Eq. (12) has values only for the last two components of macroscopic flow variables $\boldsymbol{W}_i$, indicating energy exchange between molecular translation, rotation and vibration.

Based on the fluxes, the conservative flow variables $\rho^{n+1}, (\rho \boldsymbol{U})^{n+1}, (\rho E)^{n+1}$ can be updated directly. Then λ_M^{n+1}, $(\rho E_r^M)^{n+1}$ and $(\rho E_v^M)^{n+1}$ can be obtained from the updated conservative flow variables by Eq. (14), and the vibrational energy $(\rho E_v)^{n+1}$ with implicit source term can be solved in an explicit way without iterations

$$(\rho E_v)^{n+1} = \left(1 + \frac{\Delta t}{2Z_v\tau}\right)^{-1}\left[(\rho E_v)^{\dagger} + \frac{\Delta t}{2}\left(s_v^n + \frac{(\rho E_v^M)^{n+1}}{Z_v \tau}\right)\right]. \tag{16}$$

Similarly, λ_{tr}^{n+1} and $(\rho E_r^{tr})^{n+1}$ can be obtained by Eq. (13) with the updated $(\rho E_v)^{n+1}$, then the rotational energy $(\rho E_r)^{n+1}$ can be renewed by

$$(\rho E_r)^{n+1} = \left(1 + \frac{\Delta t}{2Z_r\tau}\right)^{-1}\left[(\rho E_r)^{\dagger} + \frac{\Delta t}{2}\left(s_r^n + \frac{(\rho E_r^{tr})^{n+1}}{Z_r \tau} + \frac{(\rho E_r^M)^{n+1} - (\rho E_r^{tr})^{n+1}}{Z_v \tau}\right)\right]. \tag{17}$$

Here $(\rho E_v)^{\dagger}$ and $(\rho E_r)^{\dagger}$ are the updated intermediate vibrational and rotational energies with inclusion of the fluxes only. It would be noticed that in Eq. (14) the vibrational degrees of freedom $K_v(\lambda_M)$ rely on the full equilibrium temperature λ_M. The explicit expression of λ_M cannot be given due to the complexity of function $K_v(\lambda_M)$. In the current study, λ_M is computed by iterations

$$\lambda_M^{i+1} = \frac{\left[K_v(\lambda_M^i) + K_r + 3\right]\rho}{4\left(\rho E - \frac{1}{2}\rho \boldsymbol{U}^2\right)} \quad \text{with} \quad \lambda_M^0 = \frac{\left(K_r + 3\right)\rho}{4\left(\rho E - \frac{1}{2}\rho \boldsymbol{U}^2\right)}.$$

Numerical tests show that the relative error can approach to $\mathcal{O}(10^{-16})$ after $5 \sim 6$ iterations.

Substitute Eq. (6) into the integral solution Eq. (5) of kinetic model equation, the time evolution of distribution function along the characteristic line can be given as

$$f(\boldsymbol{r}, t) = (1 - e^{-t/\tau}) g^*(\boldsymbol{r}', t') + e^{-t/\tau} f_0(\boldsymbol{r} - \boldsymbol{u}t),$$

where

$$\boldsymbol{r}' = \boldsymbol{u}\left(\frac{te^{-t/\tau}}{1 - e^{-t/\tau}} - \tau\right), \quad t' = \left(\frac{te^{-t/\tau}}{1 - e^{-t/\tau}} - \tau\right) + t.$$

It indicates that the collisional particles will follow the near-equilibrium state $g^*(\boldsymbol{r}', t')$ after collision within the time step $t_f < \Delta t$. With the updated macroscopic flow variables, these annihilated collisional particles within the time $t \in (t_f, \Delta t)$ can be re-sampled from the hydro-particle macroscopic quantities

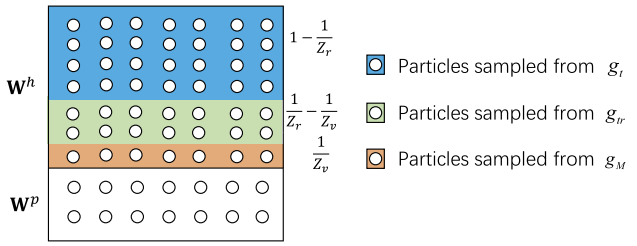

Fig. 2. Sampling particles for UGKP method with the vibrational model. (For interpretation of the colors in the figure(s), the reader is referred to the web version of this article.)

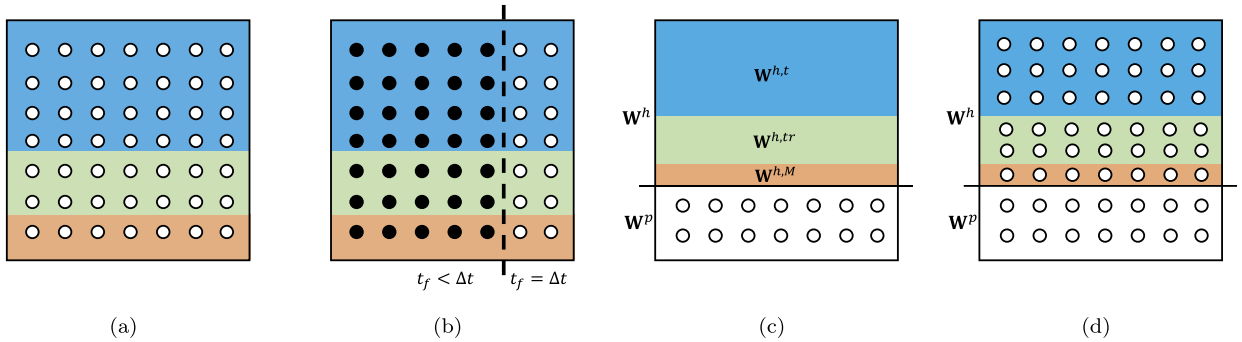

Fig. 3. Diagram to illustrate the composition of the particles during time evolution in the UGKP method. (a) Initial field, (b) classification of the collisionless particles (white circle) and collisional particles (solid circle) according to the free transport time t_f, (c) update solution at the macroscopic level, and (d) update solution at the microscopic level.

$$\boldsymbol{W}_i^{h,n+1} = \boldsymbol{W}_i^{n+1} - \boldsymbol{W}_i^{p,n+1} = \boldsymbol{W}_i^{n+1} - \frac{1}{\Omega_i} \sum_{x_k^{n+1} \in \Omega_i} \boldsymbol{\phi}_k, \tag{18}$$

where $\boldsymbol{W}_i^{p,n+1}$ is from the remaining collisionless particles in cell i. With the macroscopic quantities and the form of effective equilibrium state g^*, the corresponding particles can be generated, which is shown in Fig. 2. Details of sampling from a given distribution function are provided in Appendix B.

The free transport and collision processes for both microscopic discrete particles and macroscopic flow variables have been described above. Here, we give a summary of the procedures of the UGKP method. Following the illustration in [41], the algorithm of UGKP method for diatomic gases with molecular translation, rotation and vibration can be summarized as follows:

Step 1 For the initialization, sample particles from the given initial conditions as shown in Fig. 3(a), see Appendix B.

Step 2 Generate the free transport time t_f for each particle by Eq. (8), and classify the particles into collisionless particles (white circles in Fig. 3(b)) and collisional ones (solid circles in Fig. 3(b)). Stream the particles for free transport time by Eq. (9), and evaluate the net free streaming flux $\boldsymbol{F}_i^{fr}$ by Eq. (10).

Step 3 Reconstruct macroscopic flow variables and compute the equilibrium flux $\boldsymbol{F}_{ij}^{eq}$ by Eq. (11).

Step 4 Update the macroscopic flow variables $\boldsymbol{W}_i$ by Eqs (15), (16) and (17). Obtain the updated hydro-particle macroscopic quantities of collisional particles $\boldsymbol{W}_i^h$ by extracting the macro-quantities of remaining collisionless particles $\boldsymbol{W}_i^p$ from the total flow variables $\boldsymbol{W}_i$ in Eq. (18), as shown in Fig. 3(c).

Step 5 For the deleted collisional particles at t_f, re-sample these particles from the updated hydro-particle macroscopic variables $\boldsymbol{W}_i^h$ as shown in Fig. 3(d), as the initial state in Fig. 3(a) at the beginning of next time step.

Step 6 Go to Step 2. Continue time step evolution or stop the calculation at finishing time.

4. Unified gas-kinetic wave-particle method

In UGKP method, based on the updated hydro-particle macroscopic variables $\boldsymbol{W}_i^h$ of collisional particles, these particles will be re-sampled from equilibrium state at the beginning of next time step. However, some of these re-sampled particles will get collision in the next time step and get eliminated again. Therefore, in UGKWP method, only free transport particles in the next time step will be re-sampled from $\boldsymbol{W}_i^h$. In the continuum regime at very small Knudsen number, it is possible that no free particles will get re-sampled at all.

The collisionless particles with $t_f = \Delta t$ will be sampled from $\boldsymbol{W}_i^h$. According to the integral solution, the collisionless particles will take a fraction of $\boldsymbol{W}_i^h$ by the amount

$$\boldsymbol{W}_i^{hp} = e^{\frac{-\Delta t}{\tau}} \boldsymbol{W}_i^h.$$

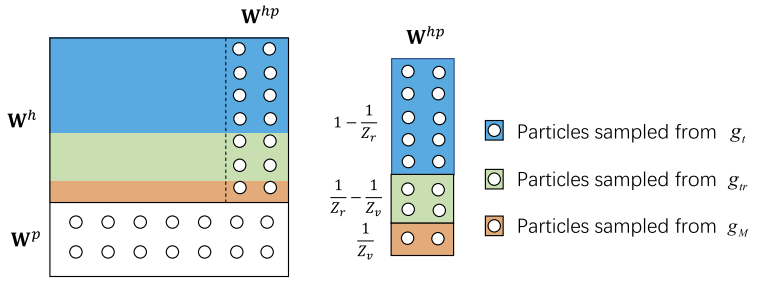

Fig. 4. Sampling particles for the UGKWP method with vibrational model.

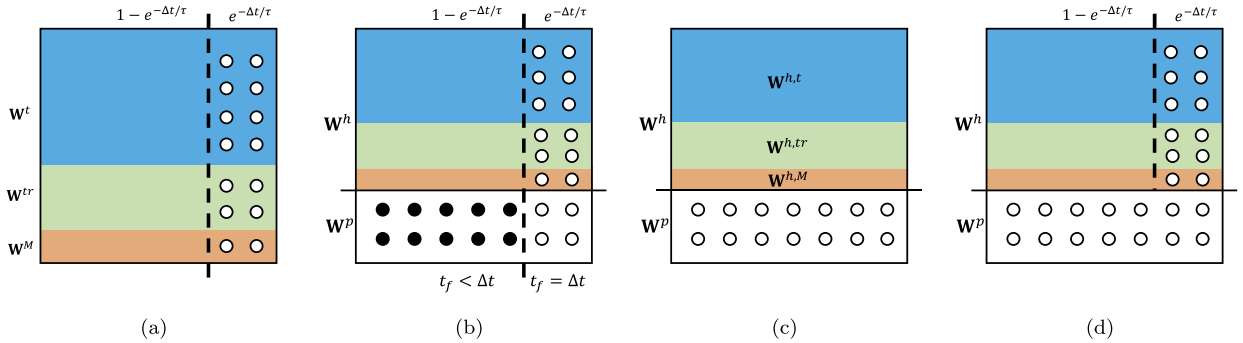

Fig. 5. Diagram to illustrate the composition of the particles during time evolution in the UGKWP method. (a) Initial field, (b) classification of the collisionless and collisional particles for $\boldsymbol{W}_i^p$, (c) update on the macroscopic level, and (d) update on the microscopic level.

As shown in Fig. 4, there is no need to sample particles from the hydrodynamic part ($\boldsymbol{W}_i^h - \boldsymbol{W}_i^{hp}$). The free transport flux from these un-sampled collisional particles can be evaluated analytically

$$\boldsymbol{F}_{ij}^{fr,h} = \int \boldsymbol{u}\cdot\boldsymbol{n}_{ij}\left[C_4' g_0^* + C_5'\boldsymbol{u}\cdot\frac{\partial g_t}{\partial \boldsymbol{r}}\right]\boldsymbol{\psi}\mathrm{d}\Xi, \tag{19}$$

where

$$C_4' = \frac{\tau}{\Delta t}\left(1-e^{-\Delta t/\tau}\right) - e^{-\Delta t/\tau},$$

$$C_5' = \tau e^{-\Delta t/\tau} - \frac{\tau^2}{\Delta t}(1-e^{-\Delta t/\tau}) + \frac{1}{2}\Delta t e^{-\Delta t/\tau}.$$

Then, the update of macroscopic flow variables in the UGKWP method becomes

$$\boldsymbol{W}_i^{n+1} = \boldsymbol{W}_i^n - \frac{\Delta t}{\Omega_i}\sum_{j\in N(i)}\boldsymbol{F}_{ij}^{eq}\mathcal{A}_{ij} - \frac{\Delta t}{\Omega_i}\sum_{j\in N(i)}\boldsymbol{F}_{ij}^{fr,h}\mathcal{A}_{ij} - \frac{\Delta t}{\Omega_i}\boldsymbol{F}_i^{fr,p} + \boldsymbol{S}_i. \tag{20}$$

The algorithm of the UGKWP method for diatomic gases can be summarized as follows.

Step 1 For the initialization, sample collisionless particles from $\boldsymbol{W}_i^{hp}$ with $t_f = \Delta t$ by Appendix B as shown in Fig. 5(a). For the first step, $\boldsymbol{W}_i^h = \boldsymbol{W}_i^{n=0}$.

Step 2 Generate the free transport time t_f by Eq. (8) for the remaining particles from previous step with total amount $\boldsymbol{W}_i^p$, and classify the particles into collisionless particles (white circles in Fig. 5(b)) and collisional ones (solid circles in Fig. 5(b)). Stream the particles for free transport time by Eq. (9), and evaluate the net free streaming flux $\boldsymbol{F}_i^{fr}$ by Eq. (10).

Step 3 Reconstruct macroscopic flow variables and compute the free transport flux of collisional particles $\boldsymbol{F}_{ij}^{fr,h}$ by Eq. (19) and the equilibrium flux $\boldsymbol{F}_{ij}^{eq}$ by Eq. (11).

Step 4 Update the macroscopic flow variables $\boldsymbol{W}_i$ by Eqs (20), (16), and (17). Delete the collisional particles at t_f ($t_f < \Delta t$). Obtain the updated macroscopic quantities for collisional particles $\boldsymbol{W}_i^h$ by extracting the macro-quantities of remaining collisionless particles $\boldsymbol{W}_i^p$ from the total flow variables $\boldsymbol{W}_i$ in Eq. (18) as shown in Fig. 5(c).

Step 5 Besides the remaining particles, re-sample the collisionless particles from $\boldsymbol{W}_i^{hp}$ with $t_f = \Delta t$ at the beginning of next time step, as shown in Fig. 5(d).

Step 6 Go to Step 2, continue time evolution or stop the calculation.

The UGKP method uses particles to represent the gas distribution function. However, the UGKWP method adopts a hybrid formulation of wave and particles to recover the gas distribution function. The wave representation of the equilibrium part can be

described by the corresponding macroscopic flow variables without sampling these particles explicitly. The non-equilibrium part is represented by surviving particles. It is realized that in the rarefied regime, the UGKWP method is dominated by particle evolution, which results in a particle method. While in the continuum regime, the UGKWP method is mainly about the evolution of macroscopic variables, and the scheme becomes a hydrodynamic NS solver, the so-called gas-kinetic scheme (GKS) [45]. Therefore, the UGKWP achieves much better computational efficiency and lower memory consumption than the purely particle methods in the transition and continuum flow regimes, and gives more accurate physical solutions than the NS solvers in the non-equilibrium regime.

5. Numerical validation

In this section, the UGKWP method with molecular vibration (WP-vib) will be used in the following test cases. Multiscale simulations across all flow regimes will be validated using Sod tube tests at Knudsen numbers ranging from 10^{-4} to 10, and the method's capacity to capture significant non-equilibrium effects in the vibrational mode will be demonstrated by simulating shock structures. The WP-vib method's computational accuracy in hypersonic flow will be quantitatively evidenced through flow simulations around a cylinder. The scheme's precision will be further affirmed by examining flow across a sphere. The capability to handle flow simulations involving complex geometries under pyramid and tetrahedral meshes will be showcased through a study of flow around a space vehicle.

Since most of the cases are external flow, the determination of the initial condition of free stream at different Knudsen number will be provided here first. For a specific gas, the density in the free stream corresponding to a given Knudsen number is given by

$$\rho = \frac{4\alpha(5-2\omega)(7-2\omega)}{5(\alpha+1)(\alpha+2)}\sqrt{\frac{m}{2\pi k_B T}}\frac{\mu}{L_{ref}\mathrm{Kn}},$$

where m is the molecular mass and L_{ref} is the reference length to define the Knudsen number. The dynamic viscosity is calculated from the translational temperature by the power law

$$\mu = \mu_{ref}\left(\frac{T}{T_{ref}}\right)^{\omega},$$

where μ_{ref} is the reference dynamic viscosity at the temperature T_{ref}.

In the tests, diatomic gas of nitrogen gas is employed with molecular mass $m = 4.65\times10^{-26}$ kg, $\alpha = 1.0$, $\omega = 0.74$, and the reference dynamic viscosity $\mu_{ref} = 1.65\times10^{-5}$ Nsm^{-2} at the temperature $T_{ref} = 273$ K. For non-dimensional cases, the freestream or upstream values are used to non-dimensionalize the flow variables, i.e.,

$$\rho_0 = \rho_\infty, \quad U_0 = \sqrt{2k_B T_\infty/m},$$
$$T_0 = T_\infty, \quad \text{or} \quad p_0 = p_\infty.$$

In addition, according to the reference [64], the vibrational collision number can be evaluated by

$$Z_v = \frac{5}{5+K_v(\lambda_v)}\frac{C_1}{T_t^{\omega}}\exp\left(C_2 T_t^{-1/3}\right), \tag{21}$$

and the rotational collision number is computed by

$$Z_r = \frac{Z_v}{Z_v + Z_r^{DSMC}}, \tag{22}$$

with

$$Z_r^{DSMC} = \frac{3}{5}\frac{Z_r^{\infty}}{1+(\sqrt{\pi}/2)\left(\sqrt{T^*/T_t}\right)+(T^*/T_t)(\pi^2/4+\pi)},$$

where $C_1 = 6.5$ and $C_2 = 220.0$ are adopted.

5.1. Shock tube test

The Sod shock tube problem is computed at different Knudsen numbers to verify the capability of the UGKWP method for simulating the continuum and rarefied flows. The non-dimensional initial condition is

$$(\rho, U, V, W, p) = \begin{cases} (1,0,0,0,1), & 0 < x < 0.5, \\ (0.125,0,0,0,0.1), & 0.5 < x < 1. \end{cases}$$

The spatial discretization is carried out by a three-dimensional structured mesh with $100\times5\times5$ uniform cells. The inlet and outlet of the tube are treated as far field, and the side walls are set as symmetric planes. The Courant–Friedrichs–Lewy (CFL) number is taken as 0.5. Constant values of $Z_r = 3.5$ and $Z_v = 10$ are used for all cases. The results at the time $t = 0.12$ are investigated.

The density, velocity as well as the temperatures including the translational, rotational, vibrational and the average temperatures obtained by WP-vib and UGKS at different Knudsen numbers are plotted in Fig. 6–8. In the calculation, the preset reference number of particles are $N_r = 2\times10^4$, 2×10^4 and 400 for the cases at Kn = 10, 0.1, and 10^{-4}, respectively. Sufficient simulation particles are

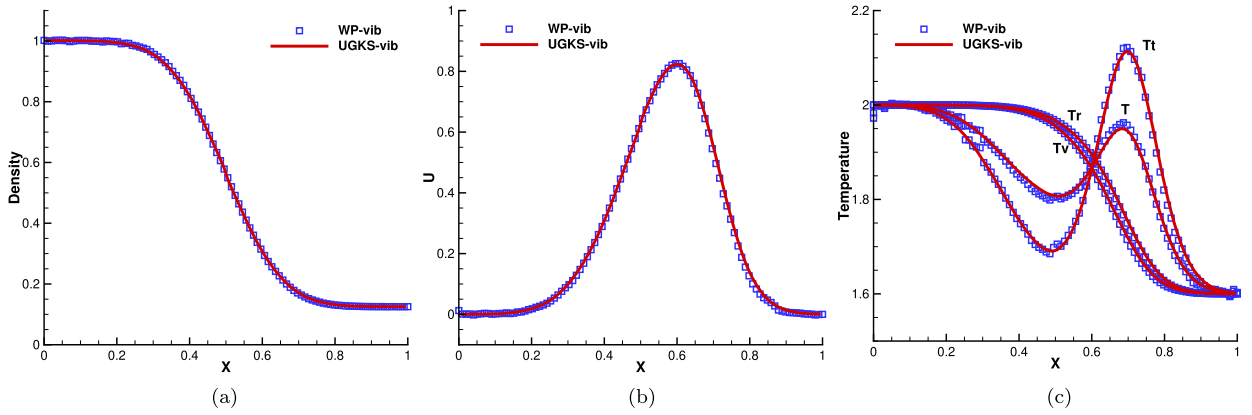

Fig. 6. Shock tube test at Kn = 10. (a) Density, (b) velocity, and (c) temperatures, compared with UGKS results using the same vibrational relaxation model.

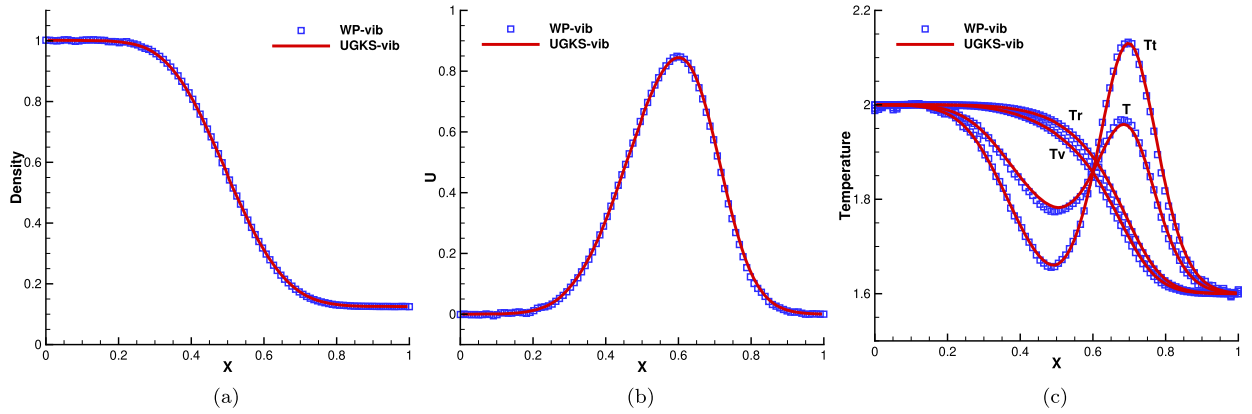

Fig. 7. Shock tube test at Kn = 0.1. (a) Density, (b) velocity, and (c) temperatures, compared with the UGKS results using the same vibrational relaxation model.

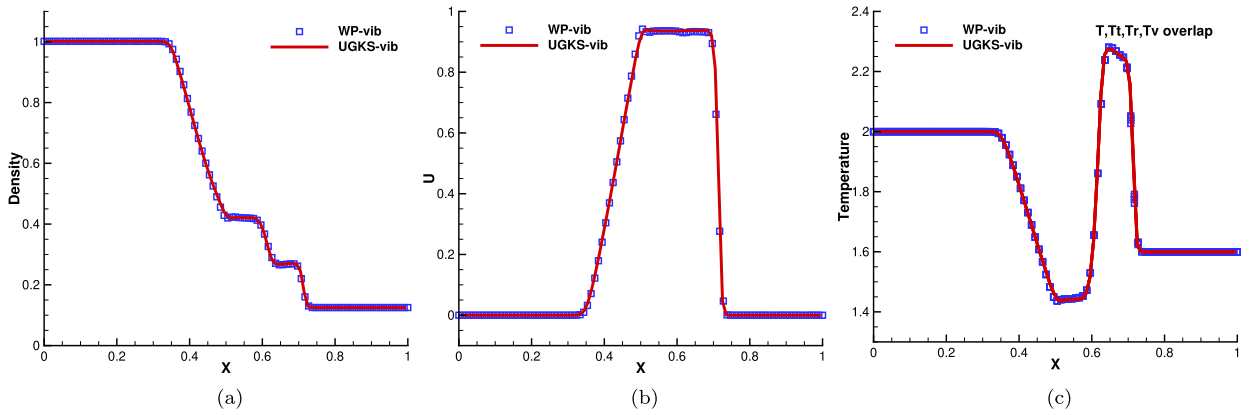

Fig. 8. Shock tube test at Kn = 10^{-4}. (a) Density, (b) velocity, and (c) temperatures, compared with the UGKS results using the same vibrational relaxation model.

employed so that satisfactory solutions are obtained with no need of time-averaging for the unsteady flow. The three-dimensional flow field obtained by the WP-vib is projected to the x direction by taking average over the cells on y-z plane to further reduce the statistical noises. For all these cases, the WP-vib results agree well with the UGKS solutions with the same vibrational relaxation model. It has been shown that the WP-vib is capable of numerical simulations in both continuum and rarefied regimes.

5.2. Shock structure

For diatomic gas with vibrational degrees of freedom, the initial condition of the normal shock wave in the upstream and downstream with different specific heat ratios is determined by the conservation, which is given in Appendix C. The computational

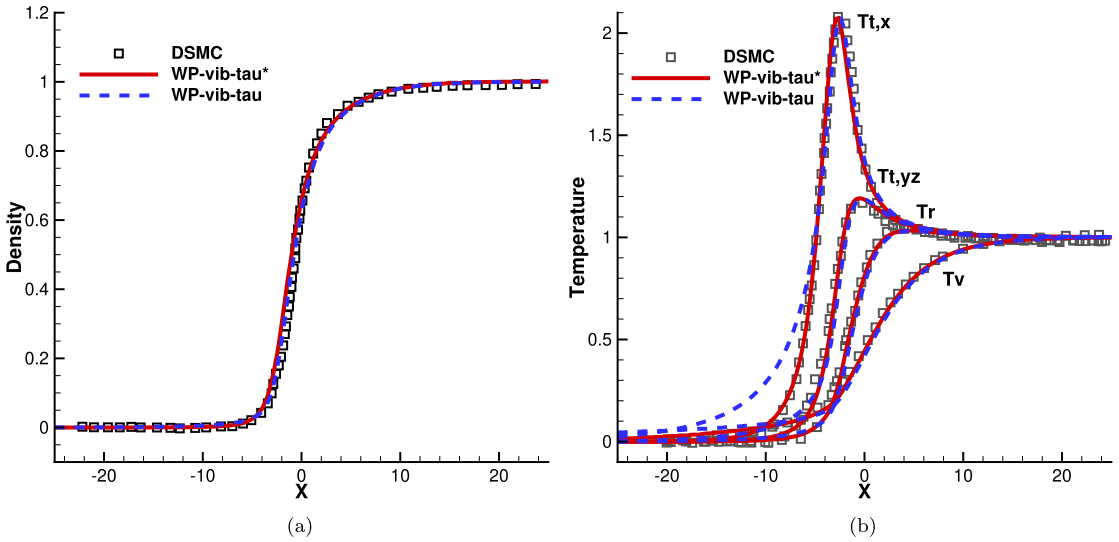

Fig. 9. Shock structure at Ma = 10. (a) Density and (b) temperatures, compared with the DSMC results.

domain $[-25, 25]$ has a length of 50 times of the particle mean free path and is divided by 200 cells uniformly. The left and right boundaries are treated as far field condition. The CFL number is taken as 0.5.

In this study, a strong shock wave at upstream Mach number $\mathrm{Ma}_1 = 10$ is investigated, and the upstream temperature is $T_1 = 226.149$ K. The rest parameters could be obtained from the non-dimensional initial condition

$$\begin{cases} \rho_1 = 1, \quad U_1 = 8.3666, \lambda_1 = 1, & x < 0, \\ \rho_2 = 6.9294, U_2 = 1.2074, \lambda_2 = 0.05736, & x \geq 0. \end{cases}$$

The rotational and vibrational collision numbers keep constant as $Z_r = 5$ and $Z_v = 28$.

In kinetic theory, the particle collision time depends on the particle velocity. In order to cope with this physical reality, the relaxation time of the high-speed particles is amended by [65]

$$\tau^* = \begin{cases} \tau, & \text{if } |\boldsymbol{u} - \boldsymbol{U}| \leq b\sqrt{RT}, \\ \frac{1}{1+a^*|\boldsymbol{u}-\boldsymbol{U}|/\sqrt{RT}}\tau, & \text{if } |\boldsymbol{u} - \boldsymbol{U}| > b\sqrt{RT}, \end{cases}$$

with two parameters $a = 0.1$ and $b = 5$.

To reduce the statistical noise, 5×10^3 simulation particles are used in each cell. The time-averaging is taken from 2500th step over 12500 steps. The normalized density and temperature from the original WP-vib, the modified WP-vib with τ^*, and the DSMC [66] simulation are plotted in Fig. 9, which show good agreement between WP-vib and DSMC data.

In Fig. 9(b), T_r and T_v denote rotational and vibrational temperature respectively. $T_{t,x}$ denotes the translational temperature in x direction, and $T_{t,yz}$ is the average translational temperature in y and z directions, which are defined by

$$T_{t,x} = \frac{1}{\rho R}\int (u - U)^2 f \mathrm{d}\boldsymbol{\Xi},$$

and

$$T_{t,yz} = \frac{1}{2\rho R}\int \left[(v - V)^2 + (w - W)^2\right] f \mathrm{d}\boldsymbol{\Xi}.$$

To further validate the WP-vib, the shock structure at Ma = 4 and Ma = 15 with the same parameters set as Ma = 10 case and with the same relaxation time τ are simulated. Fig. 10 and Fig. 11 show that the agreement in the results from UGKS and UGKWP methods.

5.3. Flow around a circular cylinder

High-speed flow passing over a semi-circular cylinder at a Mach number 15 and Kn = 0.01 is simulated [67]. The diameter of the cylinder $D = 0.08$ m. The Knudsen number is defined with respect to the diameter. The computational domain is discretized by $280 \times 200 \times 1$ quadrilateral cells. The initial reference number of particles N_r is set as 2000. The initial temperature of free stream gives $T_\infty = 217.5$ K, and the isothermal wall temperature is fixed at $T_w = 1000$ K. The rotational and vibrational collision numbers are

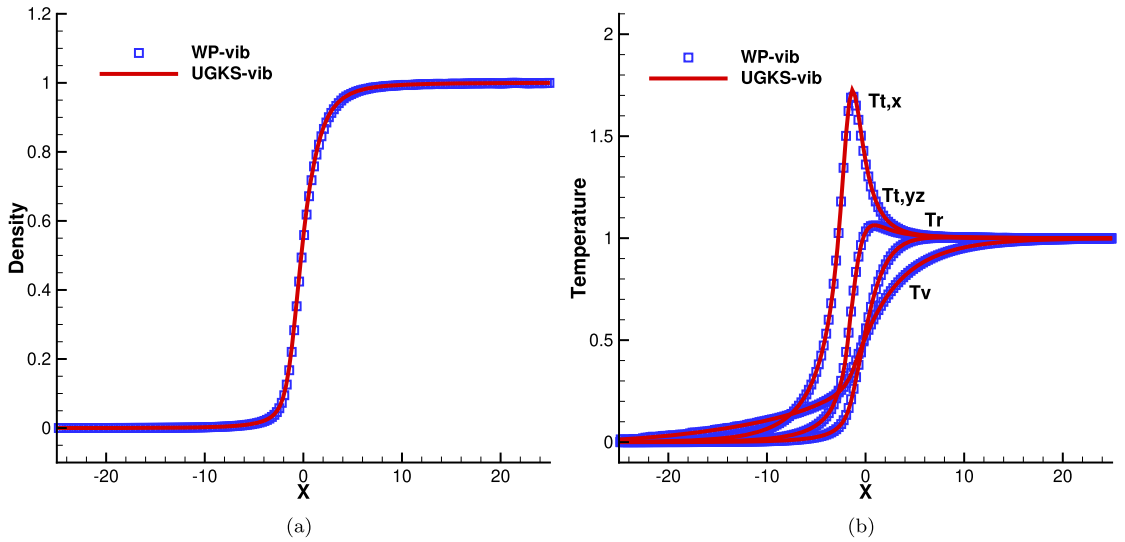

Fig. 10. Shock structure at Ma = 4. (a) Density and (b) temperatures, compared with the UGKS results using the same vibrational model.

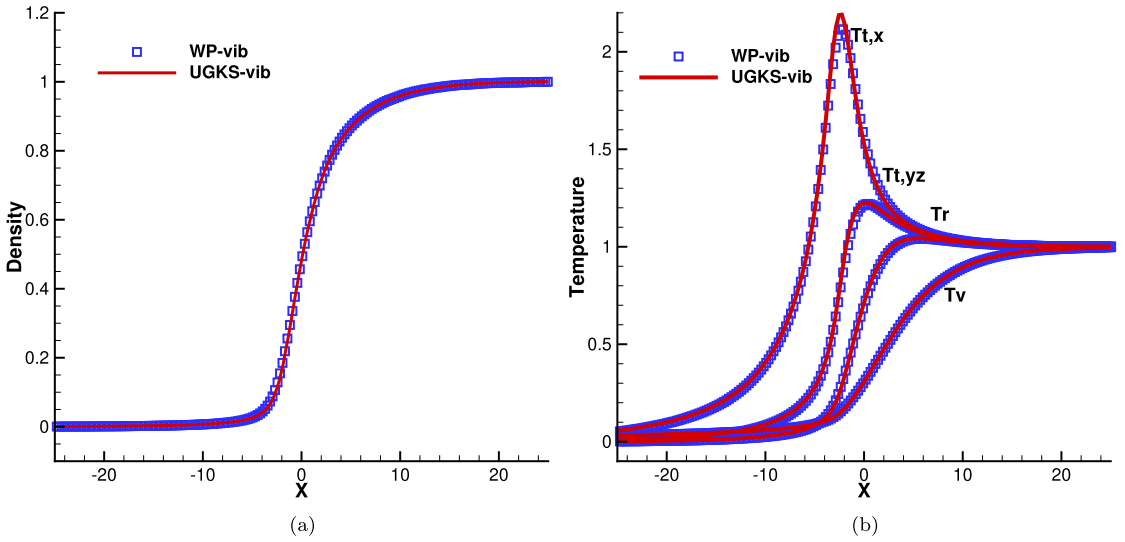

Fig. 11. Shock structure at Ma = 15. (a) Density and (b) temperatures, compared with the UGKS results using the same vibrational model.

evaluated by Eq. (22) and Eq. (21) with $Z_r^{\infty} = 12.5$ and $T^* = 91.5$ K. The CFL number is taken as 0.5. Fig. 12 plots the contours of flow field computed by WP-vib, where an initial flow field provided by 10000 steps of GKS calculation [45] is adopted, and 60000 steps of averaging have been carried out starting from the 10000th step. Fig. 13 shows the results from the WP-vib and DSMC method for the translational, rotational, and vibrational temperatures extracted along the 45° line in the upstream direction. Accepted results have been obtained by the WP-vib.

5.4. Flow around a sphere

Supersonic flow at Ma = 4.25 passing over a three-dimensional sphere in the transition regime at Kn = 0.031 is computed for nitrogen gas. The reference length is chosen as the diameter of the sphere, i.e., $D = 2 \times 10^{-3}$ m, for the definition of Knudsen number.

The initial condition for free stream is $T_{\infty} = 65$ K. Isothermal wall boundary condition at a constant temperature $T_w = 302$ K is used. Constant values of $Z_r = 3.5$ and $Z_v = 10$ are adopted in this calculation. The surface mesh of the sphere is divided into 6 blocks with 16×16 points in each block. The wall distance of the first layer of cells is 6.255×10^{-5} m.

In the calculation, the reference number of particles per cell is set at $N_r = 800$. An initial flow field provided by 500 steps of GKS calculation [45] is adopted, and the time averaging for the steady solutions starts from the 2500th step up to 9500 steps. CFL = 0.5

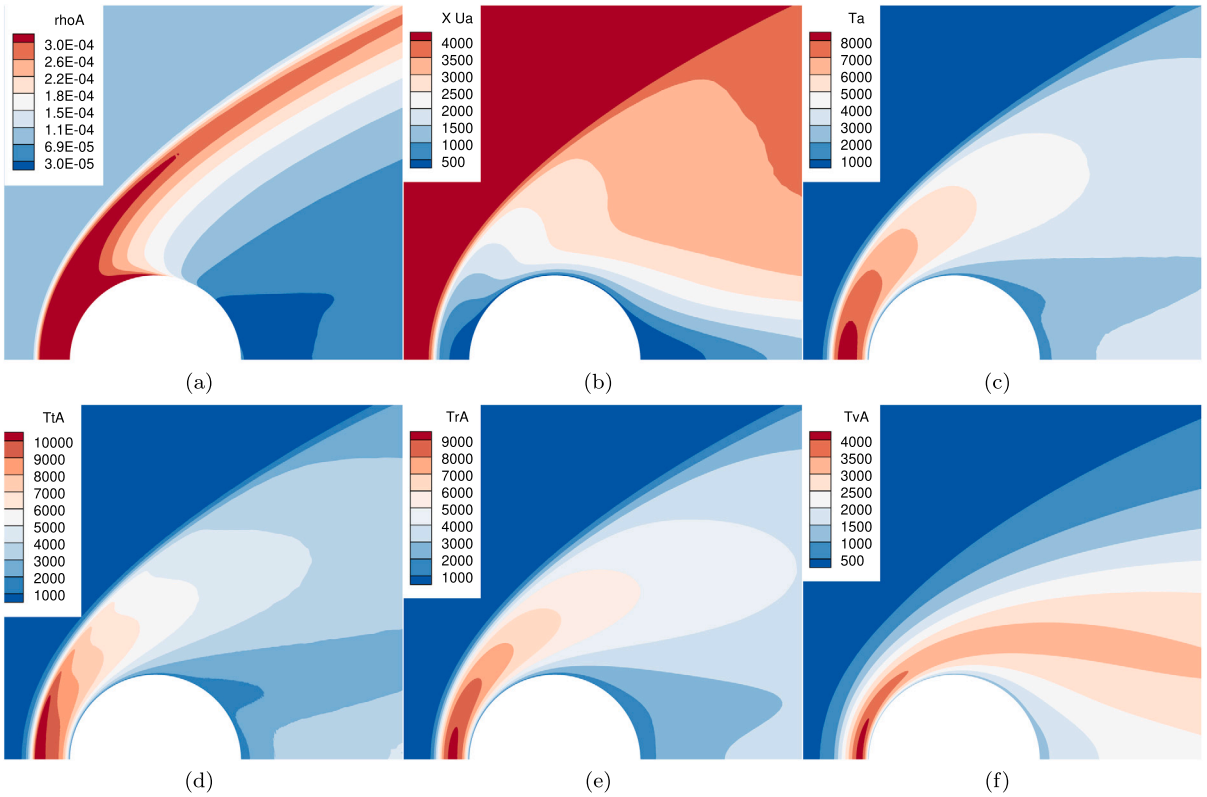

Fig. 12. Hypersonic flow at Ma = 15 around a semi-circular cylinder and Kn = 0.01. (a) Density, (b) x direction velocity, (c) temperature, (d) translational temperature, (e) rotational temperature and (f) vibrational temperature contours.

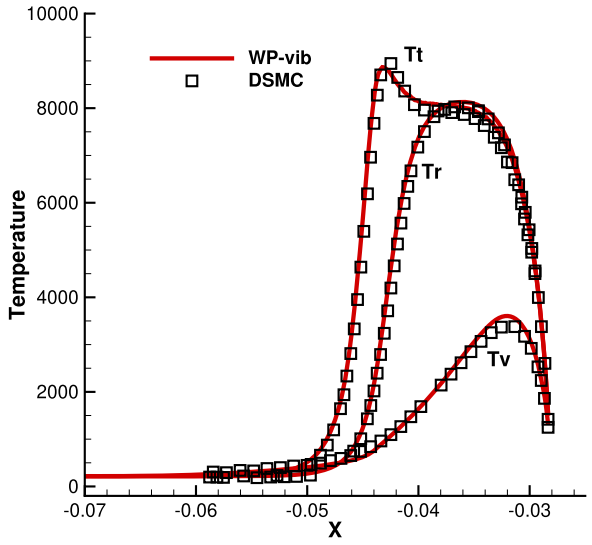

Fig. 13. Temperature distributions along the 45° extraction line at Ma = 15 and Kn = 0.01 compared with DSMC results.

is employed. The calculation takes 2 hours, running on Tianhe-2 with 2 nodes (48 cores, Intel Xeon E5-2692 v2, 2.2 GHz). The distribution of density, velocity, temperatures is shown in Fig. 14. The drag coefficient computed by the WP-vib is compared in Table 1, with those obtained from experiment (Air) [68], the UGKWP method without vibrational model, and UGKS calculation [30]. Accurate results have been obtained with a relative error smaller than 0.1%. In Fig. 15, the convergence history of the drag coefficient is plotted. For this test case, the UGKS with $40 \times 40 \times 40$ discrete velocity points needs 222.5 hours on 6 nodes (48 cores). The WP-vib shows great advantages in terms of computational efficiency and memory reduction.

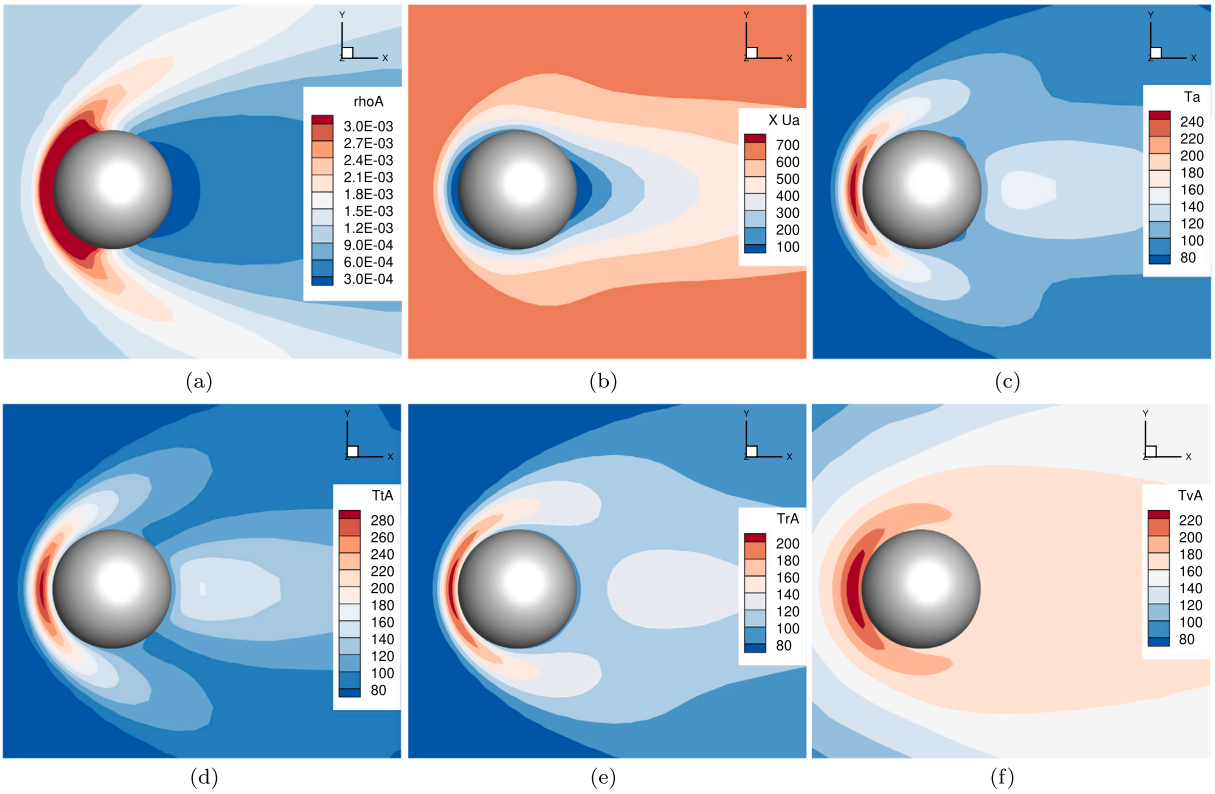

Fig. 14. Hypersonic flow at Ma = 4.25 around a sphere at Kn = 0.031. (a) Density, (b) x direction velocity, (c) temperature, (d) translational temperature, (e) rotational temperature and (f) vibrational temperature contours.

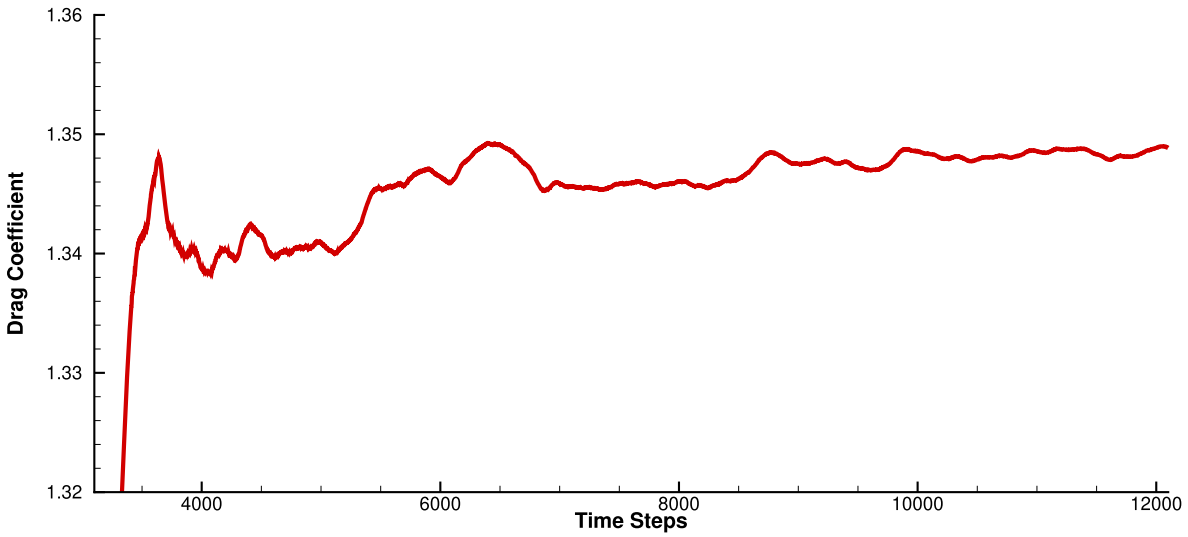

Fig. 15. Time-average process starting from 2500th step for drag coefficient of hypersonic flow around a sphere at Ma = 4.25, and Kn = 0.031.

Table 1
Comparison of the drag coefficients.

	Experiment (Air)	WP-vib (Nitrogen)	UGKWP (Nitrogen)	UGKS
C_d	1.350	1.349	1.346	1.355
Error	-	-0.03%	-0.25%	0.39%

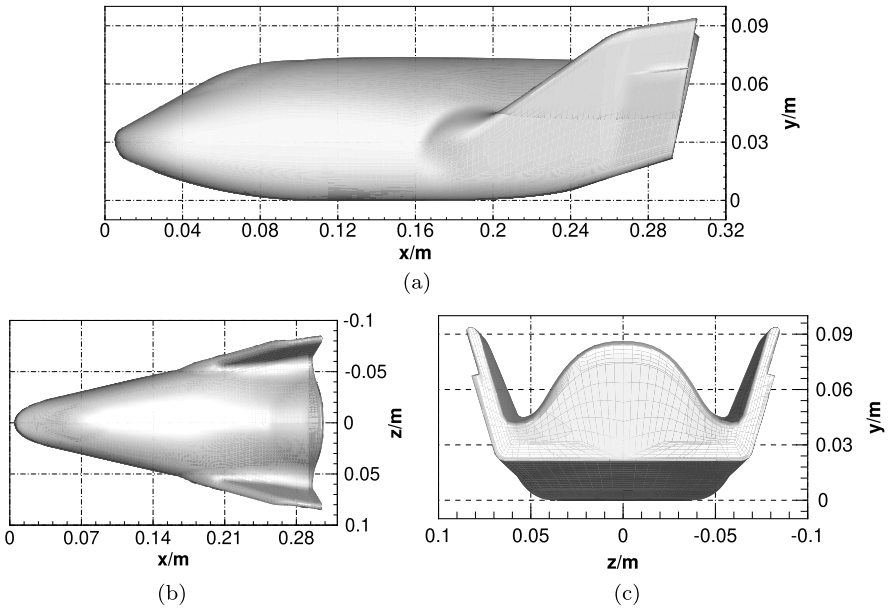

Fig. 16. Sketch of the space vehicle.

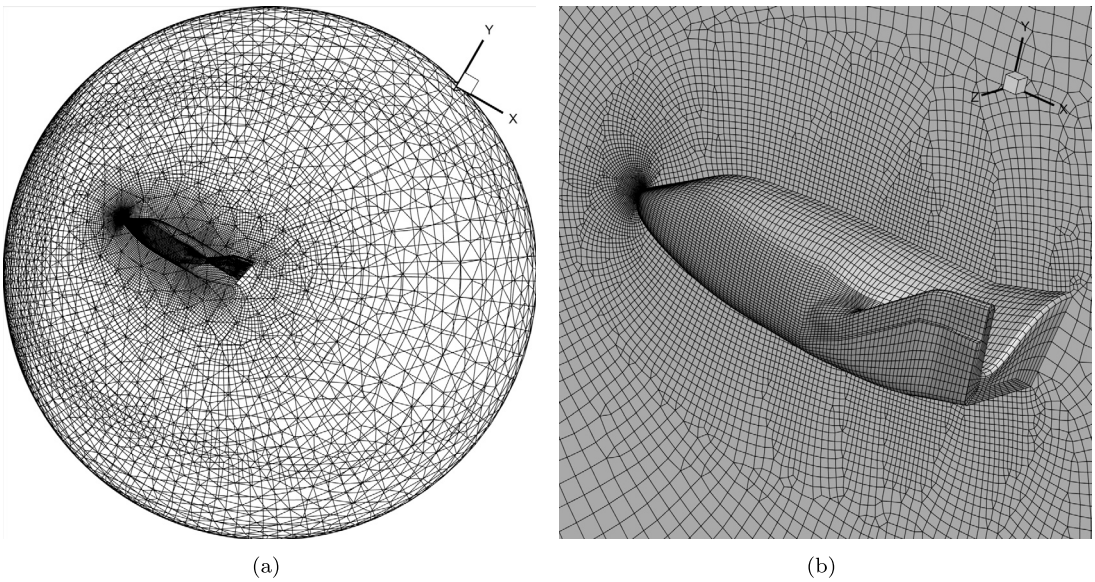

Fig. 17. Surface mesh of a space vehicle. (a) Global view and (b) local enlargement.

5.5. Flow around a space vehicle

Hypersonic flows at Ma = 6 passing over a space vehicle at $\mathrm{Kn} = 10^{-3}$ and $\mathrm{Kn} = 10^{-5}$ are simulated for nitrogen gas. According to the particle mean free path and the normal size of space vehicle (5 m), the above Knudsen numbers correspond to the flight between 50 km to 80 km altitude. These regimes can be hardly recovered by the DSMC and Navier–Stokes solutions. At the hypersonic speed, all flow regimes can emerge at different part of flying vehicle. These cases can be used to test the efficiency and capability of the WP-vib for simulating three-dimensional hypersonic flow over complex geometry in the transition regime.

The sketch of the vehicle is shown in Fig. 16. The reference length for the definition of the Knudsen number is $L_{ref} = 0.28$ m. Shown in Fig. 17, the unstructured mesh of 560593 cells consists of 15277 pyramids and 545316 tetrahedra with the minimum cell height of $L_{ref} \times 10^{-3}$ near the front of the vehicle surface. In order to have a clear understanding of the flow field, the local Knudsen number is defined as

$$\mathrm{Kn}_{GLL} = \frac{l_{mfp}}{\rho / |\nabla \rho|},$$

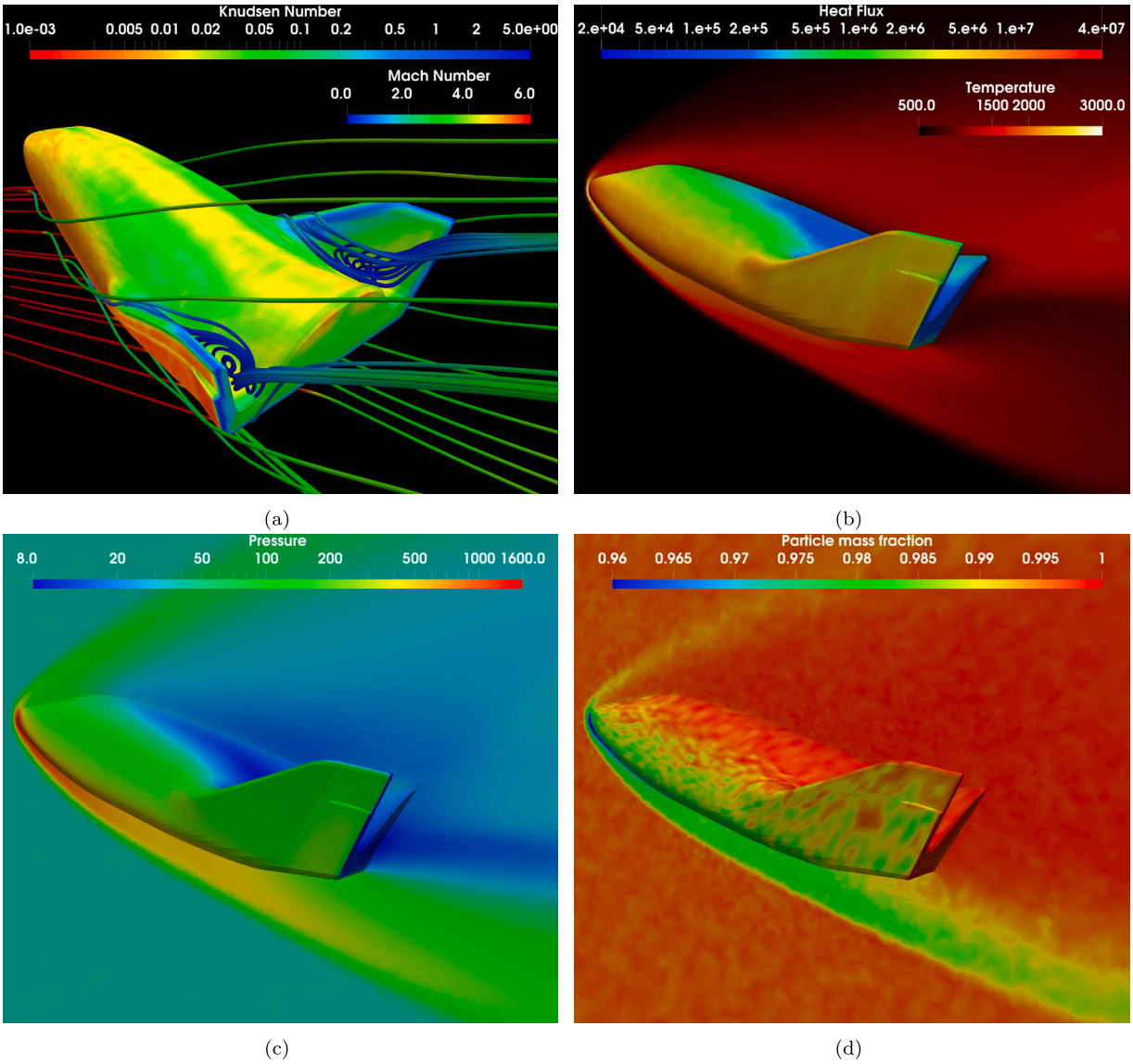

Fig. 18. Hypersonic flow at Ma = 6 around a space vehicle at $\mathrm{Kn} = 10^{-3}$. (a) Local Knudsen number Kn_{GLL} on the surface and Mach number along the streamline, (b) heat flux (vehicle surface) and temperature (outside vehicle), (c) pressure, and (d) particle mass ratio distributions.

where l_{mfp} is the local mean free path. At the same time, the local mesh Knudsen number for the determination of flow dynamics in each cell is defined by

$$\mathrm{Kn}_{mesh} = \frac{l_{mfp}}{\sqrt[3]{\Omega_i}},$$

where Ω_i is the cell volume.

The initial temperature of free stream is $T_\infty = 500$ K, and the vehicle surface is treated as isothermal wall with a constant temperature $T_w = 500$ K. The angle of attack is 30°. Constant values of $Z_r = 5$ and $Z_v = 28$ are used in the cases. The reference number of particles per cell is set as $N_r = 400$. For both $\mathrm{Kn} = 10^{-3}$ and $\mathrm{Kn} = 10^{-5}$ tests, an initial flow field calculated by GKS at 15000 steps is adopted, and the time-averaging starts from 25000th steps up to 25000 steps. CFL = 0.5 is employed.

For the case at $\mathrm{Kn} = 10^{-3}$, the distribution of local Knudsen number Kn_{GLL} around the surface of the vehicle, Mach number along the streamline, heat flux around the surface, temperature, pressure, and particle mass fraction defined by $(\rho - \rho^h)/\rho$ inside each cell are shown in Fig. 18. It can be observed from Fig. 18(a) the Kn_{GLL} has four orders of magnitude differences on the surface of vehicle. Fig. 18(d) illustrates that the particles are dominant in most parts of the computational domain.

Fig. 19 plots the distribution of the local Knudsen number and local mesh Knudsen number along the $y = 0.03$ m line on the symmetry plane in both windward and leeward (see Fig. 16). For DSMC method, the local mesh Knudsen number is restricted to

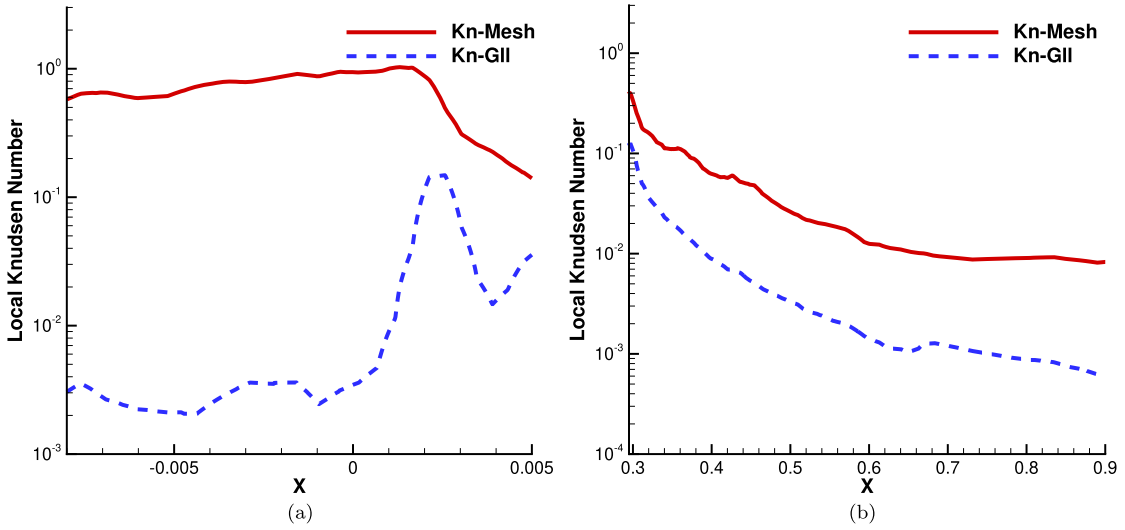

Fig. 19. Local Knudsen number distributions along the $y = 0.03$ m line on the symmetry plane at Ma = 6 and Kn = 10^{-3}. (a) Windward and (b) leeward directions.

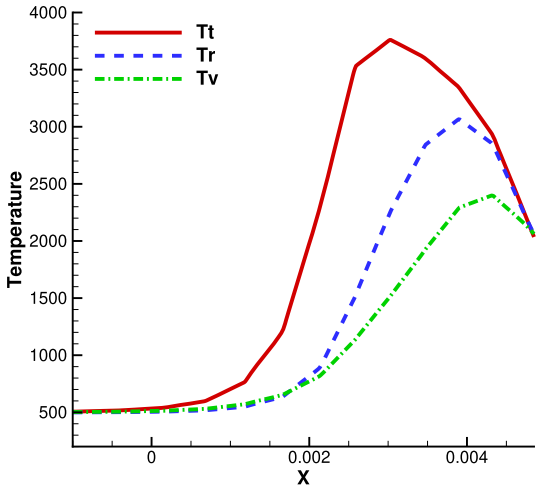

Fig. 20. Temperature distributions along the $y = 0.03$ m line on the symmetry plane at Ma = 6 and Kn = 10^{-3}.

be greater than 3, while the local mesh Knudsen number in the UGKWP method is less than 1 (see Fig. 19). The UGKWP can save significant amount of computational resources in comparison with DSMC method. Fig. 20 shows the distributions of translational, rotational and vibrational temperatures along the $y = 0.03$ m line on the symmetry plane in the front of vehicle, which displays the thermal non-equilibrium effect in the leading edge.

For the case of Kn = 10^{-5}, the distribution of local Knudsen number Kn_{GLL} around the surface of the vehicle, Mach number along the streamline, heat flux around the surface, temperature, pressure, and particle mass fraction distributions are shown in Fig. 21. Fig. 21(a) shows that in the computational domain there is still four orders of magnitude differences in local Knudsen number even at Kn = 10^{-5}. Due to the wave-particle decomposition, the particle appears only at the region with relatively large cell's Knudsen number (see Fig. 21(d)). The analytical wave and stochastic particles are dynamically coupled in each cell, which can be hardly treated by a hybrid NS-DSMC method with sub-domains separated by a buffer zone. The local Knudsen number and the local mesh Knudsen number along the $y = 0.03$ m on the symmetry plane are plotted in Fig. 22. It shows a large variation of local Knudsen number as well. The small mesh Knudsen number used in UGKWP indicates that the computational cost for the DSMC method will become unaffordable in this test. The translational, rotational, and vibrational temperatures are plotted in Fig. 23. For both cases at Kn = 10^{-3} and Kn = 10^{-5}, the simulations take 22.5 hours and 18.7 hours running on Tianhe-2 with 10 nodes (240 cores, Intel Xeon E5-2692 v2, 2.2 GHz), respectively. For UGKWP, there are no significant differences in terms of computational cost in transition regime. In order to optimize the efficiency of UGKWP method, the definition of the local Knudsen number for the determination of the wave-particle components can include the flow variable variations as well. Even in the dilute background flow region, such as the case with $Kn = 10^{-3}$, the uniform equilibrium far field background flow can be still represented and evolved by the wave component only, which saves significant amount of computational resources [69].

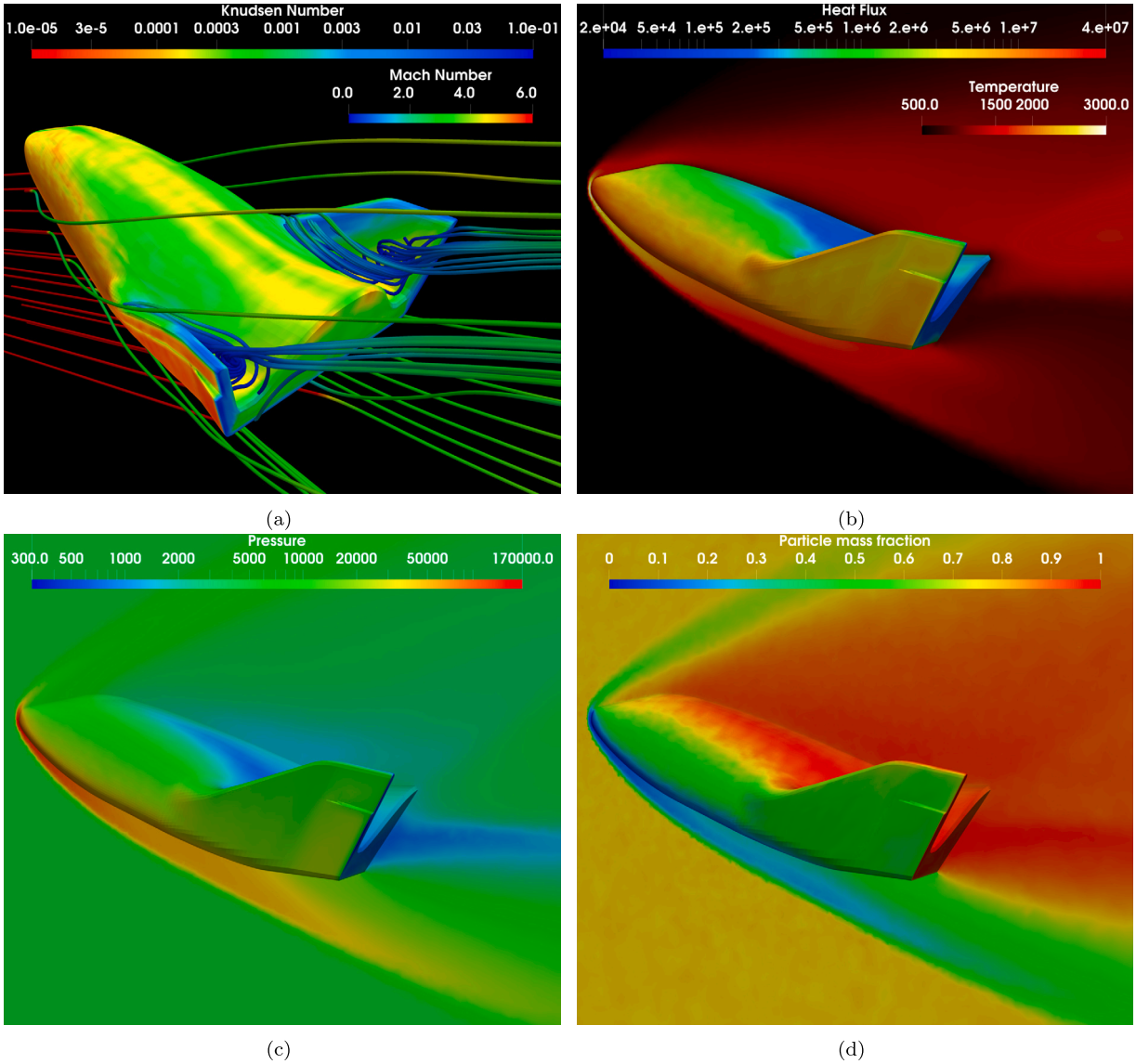

Fig. 21. Hypersonic flow at Ma = 6 around a space vehicle and Kn = 10^{-5}. (a) Local Knudsen number Kn_{GLL} on the surface and Mach number along the streamline, (b) heat flux (vehicle surface) and temperature (outside vehicle), (c) pressure, and (d) particle mass ratio distributions.

6. Conclusion

In this paper, a unified gas-kinetic wave-particle (UGKWP) method for diatomic gas with vibrational relaxation model is constructed. Different from the discrete particle velocity space based unified gas-kinetic scheme (UGKS-DVM), the UGKWP method adopts a wave-particle decomposition for capturing the evolution of the gas-distribution function. More specifically, the wave is for the description of equilibrium part in the distribution function through macroscopic variables and the particle is for the non-equilibrium one. The multiscale transport process in all Knudsen regimes is recovered through the automatic and dynamic distributions of the wave and particle decomposition. In the continuum flow regime, the UGKWP gets back to the hydrodynamic Navier–Stokes solver, the so-called gas-kinetic scheme (GKS), without introducing any particles. In the highly rarefied regime, the UGKWP becomes a purely stochastic particle method. As a result, the UGKWP can achieve a balance between the physical accuracy and numerical efficiency in the simulation of multiscale flow problem. With inclusion of molecular vibrational degrees of freedom, in this paper the UGKWP method extends its applicable regime to high-speed and high-temperature flow with the excitation of vibrational mode for the diatomic gas.

The UGKWP method is validated through many test cases and the comparison with the benchmark results from DSMC and experiments measurements. Even with the same multiscale modeling methodology as the DVM-based UGKS, the UGKWP method shows great advantages in its high computational efficiency and memory reduction due to the wave and particle representation

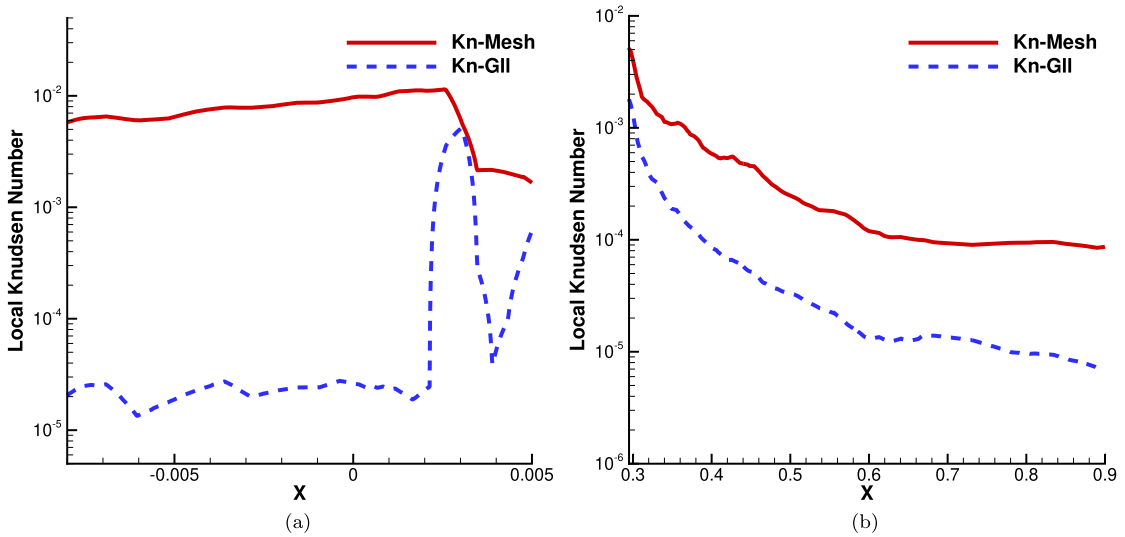

Fig. 22. Local Knudsen number distributions along the $y = 0.03$ m line on the symmetry plane at Ma = 6 and Kn = 10^{-5}. (a) Windward and (b) leeward directions.

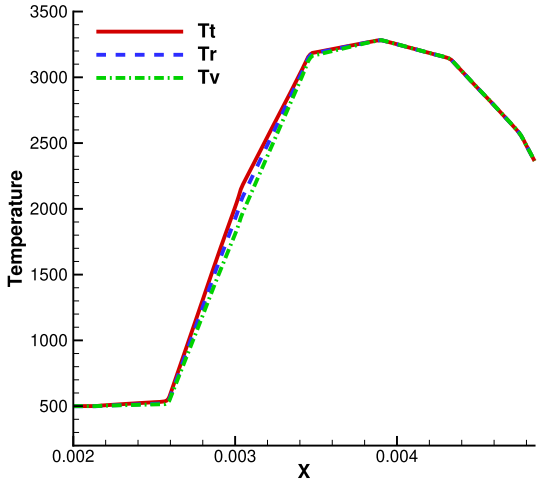

Fig. 23. Temperature distributions along the $y = 0.03$ m line on the symmetry plane at Ma = 6 and Kn = 10^{-5}.

of the gas distribution function. The UGKWP is valuable tool for the simulation of three-dimensional high-speed high-temperature rarefied and continuum flow in the aerospace applications.

CRediT authorship contribution statement

Our group has been working on the topic for a long time. The research output is coming from our joint effort. All authors read and approved the final manuscript.

Declaration of competing interest

The authors declare the following financial interests/personal relationships which may be considered as potential competing interests: Kun Xu reports financial support was provided by The Hong Kong University of Science and Technology, grant R8053.

Data availability

The data that support the findings of this study are available from the corresponding author upon reasonable request.

Acknowledgements

This work was supported by National Key R&D Program of China 2022YFA1004500, National Natural Science Foundation of China (Grant Nos. 12172316), and Hong Kong research grant council (16208021, 16301222).

Appendix A. Moments and derivative of the Maxwellian distribution function with vibrational mode

In the unified gas-kinetic wave-particle method with the vibrational mode, the equilibrium flux $\boldsymbol{F}_{ij}^{eq}$ in Eq. (11) requires higher order moments of $\boldsymbol{\xi}$ and ε_v. Here, we list the formula of the moments

$$\int_{-\infty}^{\infty} \frac{\lambda_r}{\pi} \xi^2 e^{-\lambda_r \xi^2} \mathrm{d}\xi = \frac{K_r}{2\lambda_r},$$
$$\int_{-\infty}^{\infty} \frac{\lambda_r}{\pi} \xi^4 e^{-\lambda_r \xi^2} \mathrm{d}\xi = \frac{K_r^2 + 2K_r}{4\lambda_r^2},$$
$$\int_{0}^{\infty} \frac{4\lambda_v}{K_v(\lambda_v)} \varepsilon_v e^{-\frac{4\lambda_v}{K_v(\lambda_v)}\varepsilon_v} \mathrm{d}\varepsilon_v = \frac{K_v(\lambda_v)}{4\lambda_v},$$
$$\int_{0}^{\infty} \frac{4\lambda_v}{K_v(\lambda_v)} \varepsilon_v^2 e^{-\frac{4\lambda_v}{K_v(\lambda_v)}\varepsilon_v} \mathrm{d}\varepsilon_v = 2\left(\frac{K_v(\lambda_v)}{4\lambda_v}\right)^2.$$

The distribution of the equilibrium state in space and time $(\boldsymbol{r}, t)$ can be described by the Taylor expansion

$$g^*(\boldsymbol{r}, t) = g_0 + \boldsymbol{r} \cdot \frac{\partial g}{\partial \boldsymbol{r}} + \frac{\partial g}{\partial t} t.$$

As an example, taking the $x-$ as the normal direction of the cell interface, the micro-slope a can be defined by

$$a = \frac{1}{g}\left(\frac{\partial g}{\partial x}\right),$$

with the form

$$a = a_1 + a_2 u + a_3 v + a_4 w + \frac{1}{2} a_5 \boldsymbol{u}^2 + \frac{1}{2} a_6 \boldsymbol{\xi}^2 + a_7 \varepsilon_v.$$

Applying the chain rule, the micro-slope a can be determined by the derivative of macroscopic quantities evaluated at $(\boldsymbol{r}, t)$

$$a_1 = \frac{1}{\rho}\frac{\partial \rho}{\partial x} - a_2 U - a_3 V - a_4 W - \frac{1}{2} a_5 \left(\boldsymbol{U}^2 + \frac{3}{2\lambda_t}\right) - \frac{1}{2} a_6 \frac{K_r}{2\lambda_r} - a_7 \frac{K_v(\lambda_v)}{4\lambda_v},$$
$$a_2 = \frac{\lambda_t}{\rho} R_1 - a_5 U,$$
$$a_3 = \frac{\lambda_t}{\rho} R_2 - a_5 V,$$
$$a_4 = \frac{\lambda_t}{\rho} R_3 - a_5 W,$$
$$a_5 = \frac{4\lambda_t^2}{3\rho}\left(B - U R_1 - V R_2 - W R_3\right),$$
$$a_6 = \frac{4\lambda_r^2}{K_r \rho}\left(\frac{4}{K_r}\frac{\partial(\rho E_r)}{\partial x} - \frac{1}{\lambda_r}\frac{\partial \rho}{\partial x}\right),$$
$$a_7 = \frac{4 e^{2\Theta_v R \lambda_v} \lambda_v^2}{(4\lambda_v R \Theta_v + K_v(\lambda_v))\rho}\left(\frac{4}{K_v(\lambda_V)}\frac{\partial(\rho E_v)}{\partial x} - \frac{1}{\lambda_v}\frac{\partial \rho}{\partial x}\right),$$

with the defined variables

$$B = 2\frac{\partial(\rho E - \rho E_r - \rho E_v)}{\partial x} - (\boldsymbol{U}^2 + \frac{3}{2\lambda_t})\frac{\partial \rho}{\partial x},$$
$$R_1 = 2\frac{\partial \rho U}{\partial x} - 2U\frac{\partial \rho}{\partial x},$$
$$R_2 = 2\frac{\partial \rho V}{\partial x} - 2V\frac{\partial \rho}{\partial x},$$
$$R_3 = 2\frac{\partial \rho W}{\partial x} - 2W\frac{\partial \rho}{\partial x}.$$

Appendix B. Sampling particles with vibrational mode

In the collision process, simulation particles $P_k(m_k, \boldsymbol{r}_k, \boldsymbol{u}_k, e_{r,k}, e_{v,k})$ will be resampled from a given Maxwellian distribution function to recover the gas distribution function on the microscopic level. With the primary variables $(\rho_s, \boldsymbol{U}_s, \lambda_{t,s}, \lambda_{r,s}, \lambda_{v,s})$, a Maxwellian distribution function is given by

$$g_s = \rho_s \left(\frac{\lambda_{t,s}}{\pi}\right)^{\frac{3}{2}} e^{-\lambda_{t,s}c^2} \left(\frac{\lambda_{r,s}}{\pi}\right) e^{-\lambda_{r,s}\xi^2} \frac{4\lambda_{v,s}}{K_v(\lambda_{v,s})} e^{-\frac{4\lambda_{v,s}}{K_v(\lambda_{v,s})}\epsilon_v}.$$

The microscopic translational velocity $\boldsymbol{u}_k = (u_k, v_k, w_k)^T$ for each particle can be obtained from [1]

$$\begin{aligned}
u_k &= U_s + \sqrt{-\ln(r_1)/\lambda_{t,s}}\cos(2\pi r_2),\\
v_k &= V_s + \sqrt{-\ln(r_1)/\lambda_{t,s}}\sin(2\pi r_2),\\
w_k &= W_s + \sqrt{-\ln(r_3)/\lambda_{t,s}}\cos(2\pi r_4),
\end{aligned}$$

where U_s, V_s, and W_s are the components of $\boldsymbol{U}_s$. r_1, r_2, r_3, and r_4 are independent random numbers generated from the uniform distribution between the interval $(0, 1)$. A symmetric sampling process is adopted to reduce the variance. Specifically, from a group of r_1, r_2, r_3, and r_4, a pair of simulation particles with microscopic velocity $\boldsymbol{u}_k$ and $\boldsymbol{u}'_k$ are sampled, where the symmetric microscopic velocity is

$$\begin{aligned}
u'_k &= U_s - \sqrt{-\ln(r_1)/\lambda_{t,s}}\cos(2\pi r_2),\\
v'_k &= V_s - \sqrt{-\ln(r_1)/\lambda_{t,s}}\sin(2\pi r_2),\\
w'_k &= W_s - \sqrt{-\ln(r_3)/\lambda_{t,s}}\cos(2\pi r_4).
\end{aligned}$$

Given a preset reference number N_r for each cell, the number of particles to be sampled is determined by

$$N_s = \begin{cases} 0, & \text{if } \Omega_s\rho_s \le m_{\min},\\ 2\lceil \frac{\rho_s N_r}{2(\rho - \rho^h + \rho^h e^{-\Delta t/\tau})} \rceil, & \text{if } \Omega_s\rho_s > m_{\min}, \end{cases}$$

where Ω_s is the cell volume and m_{min} is the minimum mass to sample. In the sampling process, for the cases $N_s > 0$, the mass weight actually sampled for each simulation particle is

$$m_k = \frac{\Omega_s\rho_s}{N_s},$$

which guarantees the mass density ρ_s in the volume Ω_s after the sampling process.

The rotational energy $e_{r,k}$ and vibrational energy $e_{v,k}$ for simulated particles are calculated by

$$e_{r,k} = \frac{K_r}{4\lambda_{r,s}} \quad \text{and} \quad e_{v,k} = \frac{K_v(\lambda_{v,s})}{4\lambda_{v,s}}.$$

The position $\boldsymbol{r}_k$ is derived from the uniform distribution on Ω_s. Thus far, we get all information of a simulated particle with a given Maxwellian distribution function.

In the current study, the vibrational model has the distribution function

$$g^* = \left(1 - \frac{1}{Z_r}\right) g_t + \left(\frac{1}{Z_r} - \frac{1}{Z_v}\right) g_{tr} + \left(\frac{1}{Z_v}\right) g_M,$$

which contains three Maxwellian distribution functions with different weights. Therefore, three types of simulated particles P_k^t, P_k^{tr}, and P_k^M corresponding to g_t, g_{tr}, and g_M respectively (see Fig. 2) should be sampled to recover the distribution function

$$\begin{aligned}
P_k^t &\sim \left(\rho_i^{h,t}, \boldsymbol{U}_i, \lambda_t, \lambda_r, \lambda_v\right),\\
P_k^{tr} &\sim \left(\rho_i^{h,tr}, \boldsymbol{U}_i, \lambda_{tr}, \lambda_{tr}, \lambda_v\right),\\
P_k^M &\sim \left(\rho_i^{h,M}, \boldsymbol{U}_i, \lambda_M, \lambda_M, \lambda_M\right),
\end{aligned}$$

with

$$\rho_i^{h,t} = \left(1 - \frac{1}{Z_r}\right)\rho_i^h, \quad \rho_i^{h,tr} = \left(\frac{1}{Z_r} - \frac{1}{Z_v}\right)\rho_i^h, \quad \text{and} \quad \rho_i^{h,M} = \left(\frac{1}{Z_v}\right)\rho_i^h.$$

Appendix C. Upstream and downstream condition of a shock structure with vibrational mode

Since the vibrational degrees of freedom depend on the temperature, the specific heat ratio is not a constant in the computational domain. For normal shock structure, the Rankine–Hugoniot relation under the constant specific heat ratio $\gamma = 7/5$ is no longer valid. Instead, the relation between upstream and downstream states should be obtained by imposing conservation laws with a non-constant specific heat ratio

$$\frac{\lambda_2}{\lambda_1} = \frac{\left(\mathrm{Ma}_2^2\gamma_2\right)/2 + \gamma_2/\left(\gamma_2 - 1\right)}{\left(\mathrm{Ma}_1^2\gamma_1\right)/2 + \gamma_1/\left(\gamma_1 - 1\right)}, \tag{C.1}$$

$$\frac{u_2}{u_1} = \sqrt{\frac{\left[1/2 + \mathrm{Ma}_2^2/\left(\gamma_1 - 1\right)\right]}{\left[1/2 + \mathrm{Ma}_1^2/\left(\gamma_2 - 1\right)\right]}}, \tag{C.2}$$

$$\frac{p_2}{p_1} = \frac{1 + \gamma_1\mathrm{Ma}_1^2}{1 + \gamma_2\mathrm{Ma}_2^2}, \tag{C.3}$$

$$\frac{\left(1 + \gamma_1\mathrm{Ma}_1^2\right)^2}{\gamma_1\mathrm{Ma}_1^2\left[\gamma_1/\left(\gamma_1 - 1\right) + \left(\gamma_1\mathrm{Ma}_1^2\right)/2\right]} = \frac{\left(1 + \gamma_2\mathrm{Ma}_2^2\right)^2}{\gamma_2\mathrm{Ma}_2^2\left[\gamma_2/\left(\gamma_2 - 1\right) + \left(\gamma_2\mathrm{Ma}_2^2\right)/2\right]}, \tag{C.4}$$

where the subscripts "1" and "2" denote the states at upstream and downstream, respectively. The relation between specific heat ratio and the internal degrees of freedom is

$$\gamma = \frac{7 + K_v}{5 + K_v}. \tag{C.5}$$

Substituting Eq. (2) into Eq. (C.5), the expression for specific heat ratio with respect to temperature λ can be obtained

$$\gamma = \frac{7\left(e^{2R\lambda\Theta_v} - 1\right) + 4R\lambda\Theta_v}{5\left(e^{2R\lambda\Theta_v} - 1\right) + 4R\lambda\Theta_v}. \tag{C.6}$$

Due to the complexity of Eq. (C.6), explicit determination of the flow variables at downstream is difficult, therefore, implicit iterations of Eqs (C.4), (C.1) and (C.6) are carried out to get the downstream temperature and Mach number. Then, the velocity and pressure in the downstream are determined by Eqs (C.2) and (C.3).

References

[1] G. Bird, Molecular Gas Dynamics and the Direct Simulation Monte Carlo of Gas Flows, vol. 508, Clarendon, Oxford, 1994, p. 128.
[2] I.D. Boyd, T.E. Schwartzentruber, Nonequilibrium Gas Dynamics and Molecular Simulation, vol. 42, Cambridge University Press, 2017.
[3] J. Fan, C. Shen, Statistical simulation of low-speed rarefied gas flows, J. Comput. Phys. 167 (2) (2001) 393–412.
[4] C. Shen, Rarefied Gas Dynamics: Fundamentals, Simulations and Micro Flows, Springer Science & Business Media, 2006.
[5] Q. Sun, I.D. Boyd, A direct simulation method for subsonic, microscale gas flows, J. Comput. Phys. 179 (2) (2002) 400–425.
[6] L.L. Baker, N.G. Hadjiconstantinou, Variance reduction for Monte Carlo solutions of the Boltzmann equation, Phys. Fluids 17 (5) (2005) 051703.
[7] T.M. Homolle, N.G. Hadjiconstantinou, A low-variance deviational simulation Monte Carlo for the Boltzmann equation, J. Comput. Phys. 226 (2) (2007) 2341–2358.
[8] P. Degond, G. Dimarco, L. Pareschi, The moment-guided Monte Carlo method, Int. J. Numer. Methods Fluids 67 (2) (2011) 189–213.
[9] L. Pareschi, G. Russo, Asymptotic preserving Monte Carlo methods for the Boltzmann equation, Transp. Theory Stat. Phys. 29 (3–5) (2000) 415–430.
[10] W. Ren, H. Liu, S. Jin, An asymptotic-preserving Monte Carlo method for the Boltzmann equation, J. Comput. Phys. 276 (2014) 380–404.
[11] G. Dimarco, L. Pareschi, Exponential Runge–Kutta methods for stiff kinetic equations, SIAM J. Numer. Anal. 49 (5) (2011) 2057–2077.
[12] C.K. Chu, Kinetic-theoretic description of the formation of a shock wave, Phys. Fluids 8 (1) (1965) 12–22.
[13] J. Yang, J. Huang, Rarefied flow computations using nonlinear model Boltzmann equations, J. Comput. Phys. 120 (2) (1995) 323–339.
[14] L. Mieussens, Discrete-velocity models and numerical schemes for the Boltzmann–BGK equation in plane and axisymmetric geometries, J. Comput. Phys. 162 (2) (2000) 429–466.
[15] F. Tcheremissine, Direct numerical solution of the Boltzmann equation, in: AIP Conference Proceedings, vol. 762, American Institute of Physics, 2005, pp. 677–685.
[16] V. Kolobov, R. Arslanbekov, V. Aristov, A. Frolova, S. Zabelok, Unified solver for rarefied and continuum flows with adaptive mesh and algorithm refinement, J. Comput. Phys. 223 (2) (2007) 589–608.
[17] Z. Li, H. Zhang, Gas-kinetic numerical studies of three-dimensional complex flows on spacecraft re-entry, J. Comput. Phys. 228 (4) (2009) 1116–1138.
[18] K. Xu, J. Huang, A unified gas-kinetic scheme for continuum and rarefied flows, J. Comput. Phys. 229 (20) (2010) 7747–7764.
[19] L. Wu, J. Zhang, J.M. Reese, Y. Zhang, A fast spectral method for the Boltzmann equation for monatomic gas mixtures, J. Comput. Phys. 298 (2015) 602–621.
[20] V.V. Aristov, Direct Methods for Solving the Boltzmann Equation and Study of Nonequilibrium Flows, vol. 60, Springer Science & Business Media, 2012.
[21] Z. Li, H. Zhang, Study on gas kinetic unified algorithm for flows from rarefied transition to continuum, J. Comput. Phys. 193 (2) (2004) 708–738.
[22] Z. Li, A. Peng, Q. Ma, L. Dang, X. Tang, X. Sun, Gas-kinetic unified algorithm for computable modeling of Boltzmann equation and application to aerothermodynamics for falling disintegration of uncontrolled Tiangong-No. 1 spacecraft, Adv. Aerodyn. 1 (1) (2019) 1–21.
[23] Z. Guo, K. Xu, R. Wang, Discrete unified gas kinetic scheme for all Knudsen number flows: low-speed isothermal case, Phys. Rev. B 88 (3) (2013) 033305.
[24] S. Chen, C. Zhang, L. Zhu, Z. Guo, A unified implicit scheme for kinetic model equations. Part I. Memory reduction technique, Sci. Bull. 62 (2) (2017) 119–129.
[25] S. Chen, K. Xu, A comparative study of an asymptotic preserving scheme and unified gas-kinetic scheme in continuum flow limit, J. Comput. Phys. 288 (2015) 52–65.
[26] J. Yang, J. Huang, Rarefied flow computations using nonlinear model Boltzmann equations, J. Comput. Phys. 120 (2) (1995) 323–339.
[27] Y. Zhu, C. Zhong, K. Xu, Implicit unified gas-kinetic scheme for steady state solutions in all flow regimes, J. Comput. Phys. 315 (2016) 16–38.
[28] Y. Zhu, C. Zhong, K. Xu, Unified gas-kinetic scheme with multigrid convergence for rarefied flow study, Phys. Fluids 29 (9) (2017) 096102.

[29] Y. Zhu, C. Zhong, K. Xu, An implicit unified gas-kinetic scheme for unsteady flow in all Knudsen regimes, J. Comput. Phys. 386 (2019) 190–217.
[30] D. Jiang, M. Mao, J. Li, X. Deng, An implicit parallel UGKS solver for flows covering various regimes, Adv. Aerodyn. 1 (1) (2019) 1–24.
[31] S. Chen, K. Xu, C. Lee, Q. Cai, A unified gas kinetic scheme with moving mesh and velocity space adaptation, J. Comput. Phys. 231 (20) (2012) 6643–6664.
[32] C. Mouhot, L. Pareschi, Fast algorithms for computing the Boltzmann collision operator, Math. Comput. 75 (256) (2006) 1833–1852.
[33] L. Wu, C. White, T.J. Scanlon, J.M. Reese, Y. Zhang, Deterministic numerical solutions of the Boltzmann equation using the fast spectral method, J. Comput. Phys. 250 (2013) 27–52.
[34] F. Filbet, S. Jin, A class of asymptotic-preserving schemes for kinetic equations and related problems with stiff sources, J. Comput. Phys. 229 (20) (2010) 7625–7648.
[35] G. Dimarco, L. Pareschi, Asymptotic preserving implicit-explicit Runge–Kutta methods for nonlinear kinetic equations, SIAM J. Numer. Anal. 51 (2) (2013) 1064–1087.
[36] Z. Guo, J. Li, K. Xu, Unified preserving properties of kinetic schemes, Phys. Rev. B 107 (2) (2023) 025301.
[37] Z. Guo, K. Xu, Progress of discrete unified gas-kinetic scheme for multiscale flows, Adv. Aerodyn. 3 (1) (2021) 1–42.
[38] F. Fei, J. Zhang, J. Li, Z. Liu, A unified stochastic particle Bhatnagar–Gross–Krook method for multiscale gas flows, J. Comput. Phys. 400 (2020) 108972.
[39] F. Fei, Y. Ma, J. Wu, J. Zhang, An efficient algorithm of the unified stochastic particle Bhatnagar–Gross–Krook method for the simulation of multi-scale gas flows, Adv. Aerodyn. 3 (1) (2021) 1–16.
[40] C. Liu, Y. Zhu, K. Xu, Unified gas-kinetic wave-particle methods I: continuum and rarefied gas flow, J. Comput. Phys. 401 (2020) 108977.
[41] Y. Zhu, C. Liu, C. Zhong, K. Xu, Unified gas-kinetic wave-particle methods. II. Multiscale simulation on unstructured mesh, Phys. Fluids 31 (6) (2019) 067105.
[42] K. Xu, Direct Modeling for Computational Fluid Dynamics: Construction and Application of Unified Gas-Kinetic Scheme, World Scientific, 2015.
[43] S. Liu, C. Zhong, M. Fang, Simplified unified wave-particle method with quantified model-competition mechanism for numerical calculation of multiscale flows, Phys. Rev. B 102 (2020) 013304.
[44] L. Yang, Z. Li, C. Shu, Y. Liu, W. Liu, J. Wu, Discrete unified gas-kinetic wave-particle method for flows in all flow regimes, Phys. Rev. B 108 (1) (2023) 015302.
[45] K. Xu, A gas-kinetic BGK scheme for the Navier–Stokes equations and its connection with artificial dissipation and Godunov method, J. Comput. Phys. 171 (1) (2001) 289–335.
[46] W. Li, C. Liu, Y. Zhu, J. Zhang, K. Xu, Unified gas-kinetic wave-particle methods III: multiscale photon transport, J. Comput. Phys. 408 (2020) 109280.
[47] C. Liu, K. Xu, Unified gas-kinetic wave-particle methods IV: multi-species gas mixture and plasma transport, Adv. Aerodyn. 3 (1) (2021) 1–31.
[48] X. Xu, Y. Chen, C. Liu, Z. Li, K. Xu, Unified gas-kinetic wave-particle methods V: diatomic molecular flow, J. Comput. Phys. 442 (2021) 110496.
[49] X. Yang, C. Liu, X. Ji, W. Shyy, K. Xu, Unified gas-kinetic wave-particle methods VI: disperse dilute gas-particle multiphase flow, Commun. Comput. Phys. 31 (3) (2022) 669–706.
[50] X. Yang, Y. Wei, W. Shyy, K. Xu, Unified gas-kinetic wave-particle method for three-dimensional simulation of gas-particle fluidized bed, Chem. Eng. J. (2022) 139541.
[51] P. Bhatnagar, E. Gross, M. Krook, A model for collision processes in gases. I. Small amplitude processes in charged and neutral one-component systems, Phys. Rev. 94 (3) (1954) 511–525.
[52] E. Shakhov, Generalization of the Krook kinetic relaxation equation, Fluid Dyn. 3 (5) (1968) 95–96.
[53] J. Wu, Z. Li, X. Jiang, One-dimensional shock-tube and two-dimensional plate flows in Boltzmann-Rykov Model involving rotational energy, Chin. J. Comput. Phys. 30 (3) (2013) 326–336.
[54] H. Zhang, A unified gas-kinetic scheme based on a vibrational model, Master Thesis, Northwestern Polytechnical University, 2015.
[55] S. Liu, P. Yu, K. Xu, C. Zhong, Unified gas-kinetic scheme for diatomic molecular simulations in all flow regimes, J. Comput. Phys. 259 (2014) 96–113.
[56] J. Wu, Z. Li, Z. Zhang, A. Peng, On derivation and verification of a kinetic model for quantum vibrational energy of polyatomic gases in the gas-kinetic unified algorithm, J. Comput. Phys. 435 (2021) 109938.
[57] Q. Li, J. Zeng, Z. Huang, L. Wu, Kinetic modelling of rarefied gas flows with radiation, J. Fluid Mech. 965 (2023) A13.
[58] F. Fei, Y. Hu, P. Jenny, A unified stochastic particle method based on the Bhatnagar-Gross-Krook model for polyatomic gases and its combination with DSMC, J. Comput. Phys. 471 (2022) 111640.
[59] T. Morse, Kinetic model for gases with internal degrees of freedom, Phys. Fluids 7 (2) (1964) 159–169.
[60] V. Rykov, V. Skobelkin, Macroscopic description of the motions of a gas with rotational degrees of freedom, Fluid Dyn. 13 (1) (1978) 144–147.
[61] P. Andries, P. Le Tallec, J.P. Perlat, B. Perthame, The Gaussian-BGK model of Boltzmann equation with small Prandtl number, Eur. J. Mech. B, Fluids 19 (6) (2000) 813–830.
[62] F. Bernard, A. Iollo, G. Puppo, BGK polyatomic model for rarefied flows, J. Sci. Comput. 78 (3) (2019) 1893–1916.
[63] V. Venkatakrishnan, Convergence to steady state solutions of the Euler equations on unstructured grids with limiters, J. Comput. Phys. 118 (1) (1995) 120–130.
[64] O. Tumuklu, Z. Li, D.A. Levin, Particle ellipsoidal statistical Bhatnagar–Gross–Krook approach for simulation of hypersonic shocks, AIAA J. 54 (12) (2016) 3701–3716.
[65] X. Xu, Y. Chen, K. Xu, Modeling and computation for non-equilibrium gas dynamics: beyond single relaxation time kinetic models, Phys. Fluids 33 (1) (2021) 011703.
[66] C. Cai, D.D. Liu, K. Xu, One-dimensional multiple-temperature gas-kinetic Bhatnagar–Gross–Krook scheme for shock wave computation, AIAA J. 46 (5) (2008) 1054–1062.
[67] T.R. Deschenes, I.D. Boyd, Extension of a modular particle-continuum method to vibrationally excited, hypersonic flows, AIAA J. 49 (9) (2011) 1951–1959.
[68] J.F. Wendt, Drag coefficients of spheres in hypersonic non-continuum flow, Tech. Rep. AD739250, von Karman Institute for Fluid Dynamics, 1971.
[69] Y. Wei, J. Cao, X. Ji, K. Xu, Adaptive wave-particle decomposition in UGKWP method for high-speed flow simulations, Adv. Aerodyn. 5 (25) (2023) 1–26.